Compositional patterning in irradiated alloys: Effective potentials and effective interfacial energy

Qun Li ⬤,[*] Robert S. Averback, and Pascal Bellon

Department of Materials Science and Engineering, University of Illinois at Urbana-Champaign, Urbana, Illinois 61801, USA

Compositional patterning (CP) in binary alloys during energetic particle irradiation is studied using a kinetic model that considers two competing kinetic processes, a thermally activated one promoting macroscopic phase separation (MPS) of the concentration field $c(\mathbf{r}, t)$, and a forced one resulting in finite-range random atomic mixing. The forced mixing is modeled by a Gaussian relocation distribution with a characteristic distance R. A series of approximate kinetic models are introduced by expanding the mixing function into a series of n terms, thus replacing the nonlocal evaluations of the concentration field $c(\mathbf{r}' - \mathbf{r}, t)$ by local derivatives of $c(\mathbf{r}, t)$. This approach makes it possible to obtain exact effective potentials and build steady-state diagrams for each order-n model. Phase-field (PF) simulations using these order-n models reveal that near the onset of patterning, phase evolution is accurately described using an order-3 model, which changes smoothly from an extended Cahn-Hilliard free energy in the MPS regime to a one-mode Swift-Hohenberg functional in the CP regime. Deeper into the patterning regime, higher-order models are required to achieve convergence, yielding squarelike concentration profiles characteristic of a strong segregation regime. These higher-order effective free energies are analogous to multimodal Swift-Hohenberg functionals. An alternative definition for the effective interfacial energy is proposed in the CP regime, since the interfacial area is no longer an excess quantity in that regime, precluding the use of the standard thermodynamic definition of interfacial energy.

I. INTRODUCTION

A remarkable aspect of dissipative systems is their ability to self-organize into stable, nonequilibrium microstructures [1–4]. In solid elements and alloys, for instance, irradiation with energetic particles can result in the formation of patterns comprised of voids [5,6], bubbles [7,8] and nanoprecipitates [9], while sustained plastic deformation can lead to dislocation patterning [10] as well to chemical nanolayering [11]. Modeling and simulations have established that in many of these cases, self-organization results from a dynamic competition between opposing kinetic processes. External forcing, irradiation, or plastic deformation in the above cases introduces structural and chemical disorder and drives the system into excited states, while thermally activated processes tend to promote relaxation toward lower free-energy states. For nonequilibrium systems whose overall evolution is controlled by the minimization of a potential, which then serves as a Lyapunov potential [4], the challenge is in deriving expressions of the overall, effective potential in terms of the characteristics and parameters of the competing dynamical processes [12,13]. Furthermore, self-organization into patterns raises additional questions, in particular regarding the possibility of an apparent negative interfacial energy, since patterning results in the spontaneous creation of interfaces [14].

Phase evolution in model alloys subjected to prolonged irradiation provides an excellent opportunity to systematically study these various issues, since the relevant elementary processes, such as the production of point defects and chemical disorder, are now understood on a quantitative basis; see, e.g., Ref. [15]. Earlier work by Nelson *et al.* [9] indeed established that, at moderate irradiation temperature, Ni-Al alloys form steady-state compositional patterns whose mesoscopic length scale is independent of the microstructure of the initial state. It is now known in addition that irradiation of such γ-γ' alloys at low temperatures, where forced mixing dominates the kinetics, leads to single-phase solid solutions, and at very high irradiation temperatures, where thermal diffusion dominates, macroscopic phase separation ensues [16,17]. More recent experimental studies performed for a range of dilute Cu-X alloys [18,19], where the solute X is a transition metal, established that the temperature range for patterning scales with the solute diffusion coefficient, in agreement with the above picture of competing dynamics. Moreover, recent experimental and modeling results suggest that compositional patterning can also take place in irradiated Fe-Cr alloys [20–24]. We further note, as an aside, that the patterning regime is currently of interest from the practical perspective that the microstructure in this regime is immune to coarsening of precipitates, and thus it can retain nanoscale features designed and introduced to improve the material's properties [19,25].

Modeling and simulations have provided important insights into the origins and characteristics of compositional patterning. A generic approach is to implement a kinetic model with distinct dynamics acting in parallel, here adding forced chemical mixing to the thermally activated diffusion processes [26,27]. The latter dynamics can be included using the so-called model B [28], as composition is locally
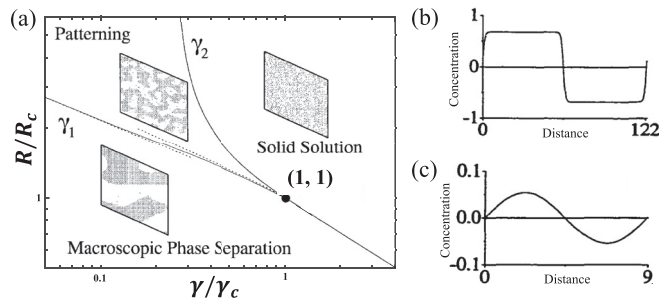

FIG. 1. (a) Steady-state phase diagram in R-γ space of an irradiated $A_{50}B_{50}$ alloy. R and γ are normalized by the critical values. γ_1 is the boundary between the MPS and CP regimes, two dashed lines are asymptotics of γ_1 in (b) for $R \gg R_c$, where CP is in SSR and the compositional profile is fitted by a square wave, and in (c) for $R \sim R_c$, where CP is in WSR and the compositional profile is fitted by a sine wave. γ_2 is the boundary between CP and SS. Insets in (a) are cuts of microstructures of 3D KMC simulations, after Ref. [27].

conserved by these dynamics. As for the mixing forced by irradiation, Martin proposed a model that randomly switched neighboring atoms, or "infinite temperature" dynamics [29], in recognition that energetic recoils are little affected by chemical interactions. Molecular dynamics have confirmed the ballistic, i.e., random, nature of the forced mixing in alloys with moderately positive heats of mixing, e.g., ≈ 0.25 eV/at or less [15,30,31]. Continuum modeling and atomistic simulations have furthermore revealed that if the jump distance for forced mixing is identical to that for thermal diffusion, i.e., one nearest-neighbor distance, compositional patterning is not possible since the outcome of the competition between the two opposing dynamics—the thermal one and the forced one—is trivially determined by the process with the largest rate. Molecular dynamics simulations of displacement collision cascades have shown, however, that when the primary recoil energies exceed ≈ 1 keV, the forced mixing extends beyond the short distance of point defect diffusional jumps [15,30,31]. Extending Martin's approach, Enrique *et al.* [32] used a phase-field model with two competing dynamics to study the effect of the finite-range mixing: The thermal dynamics employed model B, using a Ginzburg-Landau (GL) free energy, while the forced mixing was modeled using an exponential decay of recoil distances, with a decay length R. This modeling has made it possible to compute a generic steady-state phase diagram, see Fig. 1, identifying boundaries separating the regimes of macroscopic phase separation (MPS) and compositional patterning (CP), and those of patterning and solid solution (SS). Two parameters control the steady-state microstructure: (i) the relative forcing parameter $\gamma = \Gamma M$, where Γ is the rate of ballistic relocation and M is the thermally activated mobility, accelerated by the supersaturation of point defects under irradiation, and (ii) the characteristic ballistic relocation range R. It confirmed that R must exceed a critical value R_c for patterning to be possible. Furthermore, close to the critical point (γ_c, R_c) the steady-state compositional profiles take on a sinewave-like shape, corresponding to the so-called weak segregation regime (WSR), whereas deeper into the patterning regime, i.e., when $R \gg R_c$ and $\gamma > \gamma_1$ but near the γ_1 boundary, the profile resembles a square-

wave, corresponding to the strong segregation regime (SSR) [32–34]. The scaling of the dominant patterning wave vector with γ is different in these two regimes. This driven system can be characterized by an effective potential that plays the role of a Lyapunov functional for the overall system, i.e., one that continuously decreases with time [4].

Recent works have provided additional insight into the nature of such effective potentials. By linearizing the nonlinear term in the homogeneous GL free-energy density, Simeone and co-workers were able to obtain analytical solutions of the long-time evolution of the structure factor [35,36] using an asymptotic analysis. The resulting steady-state phase diagrams (see, for instance, Fig. 3 in Ref. [35]) are overall very similar to that shown in Fig. 1. Moreover, these authors were able to derive an expression for the effective potential in the patterning regime by performing a second-order Taylor expansion of the so-called response function around the patterning wave vector: It was found that the effective potential reduces to a Swift-Hohenberg (SH) one [36], thus establishing a direct connection between patterning in alloys driven by irradiation and a broad family of self-organizing systems; see, for instance, Ref. [3] for a review. It also allowed these authors to calculate steady-state phase diagrams for two-dimensional (2D) and three-dimensional (3D) systems, which are similar to those expected for a conserved SH model, and to determine the nature and symmetry of patterning states as a function of forcing parameters and alloy composition [36,37]. Several questions, however, remain unanswered for the case of alloys under irradiation. First, it is not known whether an SH effective free energy is adequate throughout the whole patterning regime since the derivation relies on a linearization of the chemical free-energy density and on a second-order Taylor expansion of the response function. Second, this derivation assumes first that the system is in a patterning regime—and thus it is not known what this effective potential becomes when the control parameters are varied in such a way that the system is taken outside of the patterning regime, for instance into the macroscopic phase-separation regime. Around that boundary, which denotes a discontinuous transition between steady states, it would be intriguing in particular to determine how the interfacial energy evolves and whether patterning can be associated with a negative interfacial energy, as suggested for other systems self-organizing into patterns; see, for instance, Refs. [38,39]. Lastly, insights into effective potentials for self-organizing dynamical systems can be obtained by considering frustrated equilibrium systems. Indeed, it has been shown that finite-range forced mixing is equivalent to introducing effective finite-range repulsive interactions between like atoms [12]. These effective interactions then compete with the (physical) attractive short-range chemical interactions present in a phase-separating system. From that perspective, a parallel can be drawn between patterning in such a dynamical system and the formation of modulated phases in equilibrium systems with frustrated physical interactions [40,41].

In this work, we specifically address the above questions using phase-field modeling based on model B dynamics with a Cahn-Hilliard (CH) free energy for the thermal dynamics and a finite Gaussian mixing for the forced mixing. The paper is organized as follows: The details of forced and thermal dynamics are introduced in Sec. II, and we define a series of

order-n kinetic models based on an expansion and truncation of the mixing terms up to order $2n$. In Sec. III we use the simplest of such models, the order-3 model, to determine the corresponding steady-state phase diagram, and we introduce an alternative definition for interfacial energy in the patterning regime. We also show that the effective free energy for that order-3 model encompasses both the CH free energy in the MPS regime and a one-mode SH free energy in the CP regime. In Sec. IV we show that far from the critical point (γ_c, R_c), higher-order kinetic models are required to reproduce the strong segregation regime. These results are then discussed in Sec. V.

II. PHASE-FIELD MODELING OF ION-BEAM MIXING UNDER IRRADIATION

A. Local model for finite-range mixing

As outlined in the Introduction, a necessary condition for irradiation induced patterning is that forced atomic mixing extends beyond a characteristic jump distance, $R > R_c$ in Fig. 1. We consider here an A-B binary alloy described by its concentration field $c(\mathbf{r}, t)$, defined as the atomic fraction of species B. The finite-range mixing rate was expressed in Ref. [32] using a nonlocal term, specifically the convolution of $c(\mathbf{r}, t)$ by the relocation distribution $\omega_R(\mathbf{r})$:

$$\left.\frac{\partial c(\mathbf{r}, t)}{\partial t}\right|_{\text{mixing}} = -\Gamma[c(\mathbf{r}, t) - \int \omega_R(\mathbf{r} - \mathbf{r}')c(\mathbf{r}', t)d\mathbf{r}']. \quad (1)$$

We introduce here an alternate formulation that expresses the finite-range forced mixing as a local term involving the concentration field $c(\mathbf{r}, t)$ and its spatial derivatives. We will show in Sec. II A that this alternate formulation offers novel physical insight, in particular regarding the question raised in the introduction about the nature of the effective potential governing the system once the thermal dynamics is included. Additionally, this approach makes it straightforward to evolve phase field equations using finite element method-based solvers, as will be illustrated in Sec. III B.

We consider here the case of a Gaussian relocation distribution $\omega_R(\mathbf{r})$. We note that Gaussian mixing is a natural model to capture atomic relocations during thermal spikes, as indicated in the MD studies on atomic mixing in displacement cascades for Cu [42], Ni [42], and NiAl [43]. Furthermore, a Gaussian model is advantageous for mathematical reasons that become clear below. The forced relocation distribution is thus taken as (m is the dimension of the space):

$$\omega_R(\mathbf{r} - \mathbf{r}') = \left(\frac{m}{2\pi R^2}\right)^{\frac{m}{2}} e^{-\frac{m|\mathbf{r}-\mathbf{r}'|^2}{2R^2}}. \quad (2)$$

The main idea here is to reexpress the mixing term by using the spatial derivatives of $c(\mathbf{r}, t)$. A simple way to do so is to consider the Fourier transform of the mixing rate,

$$\left.\frac{\partial \hat{c}(\mathbf{k}, t)}{\partial t}\right|_{\text{mixing}} = -\Gamma\left(1 - e^{\frac{-R^2 k^2}{2m}}\right)\hat{c}(\mathbf{k}, t), \quad (3)$$

where $\hat{c}(\mathbf{k}, t)$ represents the Fourier transform of the concentration field, and then to expand the k-space Gaussian in a

Taylor series,

$$\left.\frac{\partial \hat{c}(\mathbf{k}, t)}{\partial t}\right|_{\text{mixing}} = \hat{c}(\mathbf{k}, t)\sum_{p=1}^{\infty} D_p(-k^2)^p, \quad (4)$$

where the coefficients D_p are defined as

$$D_p = \Gamma\frac{R^{2p}}{(2m)^p p!}. \quad (5)$$

Next, we transform Eq. (4) back to real space to obtain the time evolution equation,

$$\left.\frac{\partial c(\mathbf{r}, t)}{\partial t}\right|_{\text{mixing}} = \sum_{p=1}^{\infty} D_p \nabla^{2p} c(\mathbf{r}, t). \quad (6)$$

It is then instructive to consider successive approximations of the mixing term by truncating the summation in Eq. (6) and retaining terms only up to $p = n$. We will refer to these approximations as order-n mixing models. This truncation is motivated by the fact that, in phase-field modeling, the compositional profile is expected to be a smooth function of position and therefore the higher-order derivatives should become increasingly less relevant. This point will be illustrated by phase-field simulations for a particular alloy model in Secs. III and IV. The order-1 model corresponds to the case of a purely diffusive forced mixing, as for instance assumed in Martin's effective temperature model for alloys under irradiation [29]. D_1 in this case would be the analog to Martin's ballistic mixing diffusion coefficient. As noted in earlier work and in the Introduction, compositional patterning does not take place in this order-1 model [44]. Higher-order terms in Eq. (6) capture the finite range of the forced mixing introduced by the relocation distribution ω_R given by Eq. (2). Note from Eq. (4) that these additional contributions should be added in pairs, so that the term with the highest power in k has a negative coefficient, ensuring that a homogeneous ideal solid solution remains stable against fluctuations of arbitrary large wave vectors. After the order-1 model, the next physically meaningful approximation to Eq. (6) is thus an order-3 model, which will be discussed in Sec. III.

We note that Eq. (6) was derived by taking advantage of the simple form of ω_R in k-space. Alternatively, one can derive Eq. (6) by performing a Taylor expansion of ω_R in real space, then iteratively applying the divergence theorem and assuming that the boundary conditions imposed on the physical domain are such that boundary integrals are null. The derivation through k-space [Eqs. (3)–(6)] is more direct and it highlights the role played by the radius of convergence of the Taylor series for a Gaussian, which is infinite; Eq. (4) is thus valid for all wave vectors $\mathbf{k}$. In contrast, if one were to consider a decaying exponential mixing function for ω_R, as in Refs. [32,35], its Fourier transform is a Lorentzian, i.e., $1/(1 + R^2 k^2)$. This function cannot be expanded into a single Taylor series with a radius of convergence spanning the full range of possible wave vectors, i.e., from $0 < k^2 R^2 < +\infty$, thus making the present approach impractical for this mixing function. Our use of a Gaussian mixing function, however, is not a serious limitation as other mixing distributions with similar physical characteristics could be used. In particular a mixing distribution that has a unique relocation distance R,

i.e., $\omega_R(\mathbf{r} - \mathbf{r}') = \delta(|\mathbf{r} - \mathbf{r}'| - R)$ could be employed with an order-n expansion since its Fourier transform is proportional to $2[1 - \cos(kR)]$, whose Taylor expansion in k-space has an infinite radius of convergence. This series is in fact very similar to the one obtained for the Gaussian mixing function, Eq. (4). Any physical mixing model, including a decaying exponential, could therefore be considered by simply decomposing it into, or approximating it with, a series of Dirac mixing distributions with suitable relocation distances.

B. An order-n extended Cahn-Hilliard model for alloys under irradiation

We add the thermal component to the evolution equation using the standard Cahn-Hilliard model [45]:

$$\frac{\partial c(\mathbf{r}, t)}{\partial t} = \left.\frac{\partial c(\mathbf{r}, t)}{\partial t}\right|_{\text{thermal}} + \left.\frac{\partial c(\mathbf{r}, t)}{\partial t}\right|_{\text{mixing}}, \quad (7)$$

$$\left.\frac{\partial c(\mathbf{r}, t)}{\partial t}\right|_{\text{thermal}} = \nabla \cdot M(c) \nabla \frac{\delta F}{\delta c}, \quad (8)$$

$$F(c) = \int_V f(c) + \frac{\kappa}{2} |\nabla c|^2 dV. \quad (9)$$

$M(c)$ is the atomic mobility, which in general depends on $c(\mathbf{r}, t)$. In this work, the atomic mobility is assumed to be a constant so that compact analytical results can be obtained. $F(c)$, the free-energy functional of the system, is comprised of a mean-field bulk free energy $f(c)$ and a gradient energy term accounting for diffuse interfaces. A regular solution model is used, $f(c) = G_B c + G_A(1-c) + \Omega c(1-c) + k_B T[c \ln c + (1-c)\ln(1-c)]$, to describe a binary immiscible alloy system. G_B (G_A) is the molar Gibbs energy for pure element B (A), Ω is the interaction parameter in kJ/mol, k_B is the Boltzmann constant, and T is the absolute temperature.

With an order-n approximation for the forced mixing, the evolution equation in real space and its linearized form in Fourier space are

$$\frac{\partial c(\mathbf{r}, t)}{\partial t} = \nabla \cdot M \nabla \left(\frac{\partial f}{\partial c} - \kappa \nabla^2 c \right) + D_1 \nabla^2 c + D_2 \nabla^4 c$$
$$+ D_3 \nabla^6 c + \cdots + D_n \nabla^{2n} c, \quad (10)$$

$$\frac{\omega(k)}{M} = -\frac{\partial^2 f}{\partial \hat{c}^2} k^2 - \kappa k^4 - \frac{D_1}{M} k^2 + \frac{D_2}{M} k^4 - \frac{D_3}{M} k^6$$
$$+ \cdots + \frac{D_n}{M} (-k^2)^n. \quad (11)$$

We refer to such a model as an order-n extended Cahn-Hilliard (ECH) model for alloys under irradiation. This terminology generalizes the one already used for thermal systems, where the addition of an inhomogeneity penalty proportional to a Laplacian square, resulting in a k^6 term in the kinetic equation in Fourier space, has been referred to as an "extended Cahn-Hilliard model [46]."

An effective free-energy-like quantity can be derived for the driven system in the form $F_{\text{eff}} = F + \gamma G$ with $\gamma = \Gamma M$ defines a forcing intensity. G is the additional free energy due to forced mixing. The time evolution of the system is then governed by

$$\frac{\partial c(\mathbf{r}, t)}{\partial t} = \nabla \cdot M \nabla \frac{\delta F_{\text{eff}}}{\delta c}. \quad (12)$$

The effective free energy for an order-n ECH model takes the following form:

$$F_{\text{eff}} = \int_V \left[f(c) - \frac{D_1}{2M} c(1-c) + \frac{\kappa - \frac{D_2}{M}}{2} |\nabla c|^2 \right.$$
$$\left. + \frac{D_3}{2M} |\nabla^2 c|^2 + \cdots + \frac{D_n}{2M} (-1)^{n-1} |\nabla^{n-1} c|^2 \right] dV \quad (13)$$

while the effective chemical potential μ_{eff} is given by

$$\mu_{\text{eff}} = \frac{\partial f(c)}{\partial c} - \kappa \nabla^2 c + \frac{D_1}{2M}(2c-1) + \frac{D_2}{M} \nabla^2 c$$
$$+ \frac{D_3}{M} \nabla^4 c + \cdots + \frac{D_n}{M} \nabla^{2(n-1)} c. \quad (14)$$

The existence of an effective free energy will make it possible to assess the relative stability of different metastable states generated by the phase field simulations presented in the next sections. Note that in the above model, point defects are not explicitly considered. It is assumed that the vacancies and interstitials created by irradiation quickly reach steady state, and thus the resulting excess of point defects can be captured by simply rescaling M, see for instance Refs. [47,48]. Elimination of these fast variables, however, excludes any possible coupling between defects and solute fluxes; these effects will be considered in future work.

III. COMPOSITIONAL PATTERNING CLOSE TO THE CRITICAL POINT: AN ORDER-3 EXTENDED CH MODEL

As indicated in Sec. II A, the diffusive order-1 model does not predict patterning, and higher-order compositional inhomogeneity terms in the order-n ECH model should be added for pattern formation. In this section, we focus on the order-3 ECH model as it is the simplest model that predicts compositional patterning; plus, it yields simple analytical expressions for the phase boundaries between CP, MPS, and SS, namely expressions for γ_1 and γ_2, the critical point of the onset of patterning (γ_c, R_c) and the wave vectors k_1, k_2. We also show that its effective free energy reduces to a one-mode SH potential inside the patterning regime. We first investigate this order-3 ECH model using a linear stability analysis in Sec. III A, and then we employ phase-field simulations in Secs. III B–III D to study the long-term evolution of the system and its steady-state microstructures. We also report on how the form of the effective free energy changes as the operating point of the system moves from MPS to CP, and we introduce an alternative definition for the effective interfacial energy in the patterning regime.

A. Linear stability analysis

The evolution equation for the order-3 ECH model is given by

$$\frac{\partial c(\mathbf{r}, t)}{\partial t} = \nabla \cdot M \nabla \left(\frac{\partial f(c)}{\partial c} - \kappa \nabla^2 c \right) + D_1 \nabla^2 c$$
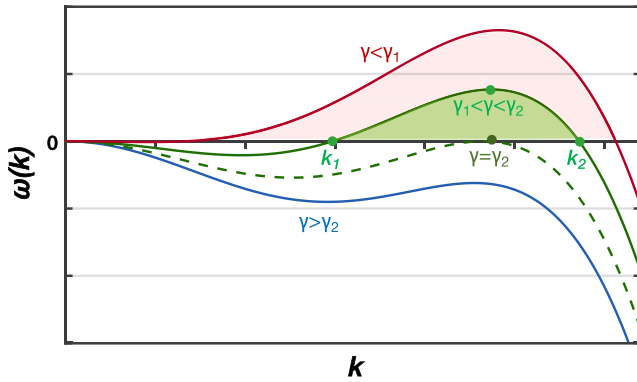$$+ D_2 \nabla^4 c + D_3 \nabla^6 c. \quad (15)$$

FIG. 2. Effect of γ on the growth rate $\omega(k)$ of perturbation wave vectors k to a homogeneous solution. The CP regime is corresponding to a window of growing wave vectors (k_1, k_2).

By grouping together terms with the same order of spatial derivative on the right-hand side of Eq. (15), an effective bulk free energy $f_{\text{bulk}}^{\text{eff}}(c)$, an effective coefficient of gradient energy κ_1^{eff}, and an effective second-order inhomogeneity coefficient κ_2^{eff} are defined as follows:

$$f_{\text{bulk}}^{\text{eff}}(c) = f(c) - \frac{D_1}{2M}c(1-c), \tag{16}$$

$$\kappa_1^{\text{eff}} = \kappa - \frac{D_2}{M}, \tag{17}$$

$$\kappa_2^{\text{eff}} = \frac{D_3}{M}. \tag{18}$$

The effective free energy and chemical potential are

$$F_{\text{eff}} = \int_V \left[f_{\text{bulk}}^{\text{eff}}(c) + \frac{\kappa_1^{\text{eff}}}{2}|\nabla c|^2 + \frac{\kappa_2^{\text{eff}}}{2}|\nabla^2 c|^2 \right] dV, \tag{19}$$

$$\mu_{\text{eff}} = \frac{\partial f_{\text{bulk}}^{\text{eff}}(c)}{\partial c} - \kappa_1^{\text{eff}}\nabla^2 c + \kappa_2^{\text{eff}}\nabla^4 c. \tag{20}$$

A linear stability analysis is performed to evaluate the response of Eq. (15) to small perturbations of the form $c(r, t) = \bar{c}(1 + \epsilon e^{\omega t + i\mathbf{k}\cdot\mathbf{r}})$. The amplification factor ω is given by

$$\frac{\omega(k)}{M} = -\frac{\partial^2 f_{\text{bulk}}^{\text{eff}}}{\partial \hat{c}^2}k^2 - \kappa_1^{\text{eff}}k^4 - \kappa_2^{\text{eff}}k^6. \tag{21}$$

In the absence of irradiation, $\frac{\partial^2 f}{\partial \hat{c}^2}$ is negative as the temperatures and compositions studied here are always such that the alloy is inside its spinodal, and κ is positive. The contributions of $\frac{D_1}{M}$ and $\frac{D_2}{M}$ to $\frac{\partial^2 f_{\text{bulk}}^{\text{eff}}}{\partial \hat{c}^2}$ and κ_1^{eff} will reduce these values significantly or even change their signs, i.e., moving the initial condition out of the spinodal decomposition region and reducing κ_1^{eff} or even making it negative. In contrast, the sign of κ_2^{eff} is always positive, ensuring that unstable wave vectors remain bounded. A general evolution of the dispersion equation $\omega(k)$ is shown in Fig. 2: for small values of γ, $\gamma < \gamma_1$, the linear instability can be classified as a stationary type II instability [3], and the characteristic wavelength of patterning diverges to infinity, as expected for macroscopic phase separation. For intermediate γ, $\gamma_1 < \gamma < \gamma_2$, there exists a band of unstable wave vectors (k_1, k_2) suggesting compositional patterning with a characteristic wavelength near $2\pi/k_c$, where

k_c is the wave vector maximizing $\omega(k)$. For larger values of γ ($\gamma \sim \gamma_2$), the system undergoes a supercritical pitchfork bifurcation and is reminiscent of a stationary type-I instability in the analysis of the Swift-Hohenberg equation [3].

Starting from the linearized evolution equation [Eq. (21)], expressions for the important boundary parameters marked in Fig. 2 can be directly derived (the superscript "linear" is added to distinguish these values from the ones pertaining to the full steady-state diagram, as in Fig. 1). First, the boundary between the MPS and CP regimes, γ_1^{linear}, is derived by $\frac{d\omega}{dk}$ changing sign at $k = 0$. The boundary between CP and SS, γ_2^{linear}, is determined by $\frac{d\omega}{dk}|_{k=k_c} = 0$ and $\omega(k_c) = 0$. The onset of patterning (γ_c, R_c) is obtained by setting $\gamma_1^{\text{linear}} = \gamma_2^{\text{linear}}$. In the patterning regime, the boundaries of the range of wave vectors with positive growth rates (k_1, k_2) are the two positive real roots of Eq. (21) (see Appendix A for details). While the above linear stability analysis provides analytical expressions defining the compositional patterning regime, it necessary to include nonlinear effects to determine the exact domain of existence of compositional patterning as well as to investigate defective patterns. We thus turn to numerical simulations of the full order-3 ECH model in the next sections.

B. Simulation methods

The phase-field (PF) equation Eq. (15) lends itself to integration by finite-element method (FEM) based solvers since it is only a function of the local composition and its spatial derivatives. Equation (15) can be rewritten with dimensionless units (here m is the dimension of the space):

$$\frac{\partial c}{\partial \tilde{t}} = \tilde{\nabla}^2 \widetilde{\mu_{\text{eff}}}, \tag{22a}$$

$$\widetilde{\mu_{\text{eff}}} = \left(1 - \frac{\tilde{\gamma}\tilde{R}^2}{4m}\right)(1 - 2c) + \tilde{T}\ln\frac{c}{1-c} - \tilde{\kappa}\tilde{\nabla}^2 c$$
$$+ \frac{\tilde{\gamma}\tilde{R}^4}{(2m)^2 2!}\tilde{\nabla}^2 c + \frac{\tilde{\gamma}\tilde{R}^6}{(2m)^3 3!}\tilde{\nabla}^4 c, \tag{22b}$$

where

$$\tilde{t} = \frac{tM\Omega}{a_0^2}, \quad \tilde{\nabla} = a_0\nabla, \quad \tilde{\gamma} = \frac{\Gamma a_0^2}{M\Omega} = \gamma\frac{a_0^2}{\Omega}, \quad \tilde{R} = \frac{R}{a_0},$$

$$\tilde{T} = \frac{k_B T}{\Omega}, \quad \tilde{\kappa} = \frac{\kappa}{\Omega a_0^2}. \tag{22c}$$

a_0 is the grid spacing in PF simulations. The dimensionless form of the effective chemical potential has four independent parameters, $\tilde{\gamma}$, $\tilde{R}$, $\tilde{T}$, and $\tilde{\kappa}$, and thus helps to assess the effects of model parameters on the evolution equation; note that (i) $\tilde{T}$ is proportional to the usual reduced temperature T/T_c in phase transition phenomena, and (ii) M is a function of T so $\tilde{\gamma}$ will be temperature-dependent as well. In this work, we focus on the effect of forcing parameters γ and R. This choice was guided by the fact that no qualitatively significant effects were observed in the PF simulations when varying $\tilde{T}$ and $\tilde{\kappa}$ around the values considered here. In particular, no new steady state or new compositional patterning regime was detected. In the present work, we use the FEM framework MOOSE [49] with adaptive meshing and time stepping to solve the PF Eq. (10); see the supplemental material [50] for more

TABLE I. Materials parameters used in the order-n ECH model.

	Atomic mobility	Nominal composition of B	Gibbs energy of pure B/A	Interaction parameter	Temperature	Coefficient of gradient energy
Symbol	M	$\bar{c}$	$G_B = G_A$	Ω	T	κ
Value	2.2841×10^{-26}	0.5	-20	17	700	8.125×10^{-16}
Unit	m^{2}mol/J/s		kJ/mol	kJ/mol	K	Jm^2/mol

information about adaptive meshing and a detailed description of weak forms and solver options in Appendix B. The atomic mobility and the coefficient of gradient energy are taken from Ref. [51] for the spinodal decomposition of Fe-Cr. The interaction parameter Ω is chosen so that the spinodal temperature for the equiatomic alloy is $T_c = 1022$ K. The complete list of materials parameters is compiled in Table I. Since the present study focuses on the equiatomic composition, it is sufficient to perform two-dimensional simulations as the most stable steady states in the patterning regime are lamellar microstructures. We refer to the A-rich and B-rich phases as α and β, respectively, Furthermore, for simplicity, we vary γ and R but keep here the temperature fixed at 700 K ($0.68T_c$). At that temperature, the equilibrium atomic fractions of B in α and β phases are 0.0786 and 0.9214, respectively. Separate simulations at other temperatures, from $0.5T_c$ to $0.75T_c$, did not reveal any qualitatively different evolutions. Lastly, since we are not interested here in the effects of surfaces or other boundaries, we use periodic boundary conditions.

C. Determination of steady states by minimization of F_{eff}

We present in this section the results of phase-field simulations of an irradiated $A_{50}B_{50}$ binary alloy using an order-3 ECH model. We focus on the patterning regime and pattern morphology near (γ_c, R_c), the onset of patterning since, as we will show in Sec. IV, the order-3 ECH model becomes inaccurate away from this point. We thus choose $R = 1.1R_c$ and

we use a γ value between γ_1^{linear} and γ_2^{linear}. The simulation domain is 30 nm $\times$ 30 nm. The initial conditions (ICs) of the simulations are either a solid solution or a phase-separated bilayer structure in order to sample broadly possible steady-state microstructures. For IC = solid solution, the nominal concentration of B is 0.5 everywhere in the domain, but local random fluctuations (with amplitude ≈ 0.05) are introduced to trigger phase decomposition. For IC = phase separation, two stripes of α and β phases are separated by a straight interface of width 0.5 nm. Under irradiation, the solid solution decomposes and forms a defective lamellar structure with dislocation-like defects [see Fig. 3(a)], while for the phase-separated system the solid solution decomposes through a series of instabilities into thinner layers, also forming a defective microstructure, in this case with a transverse long-wavelength (zigzag) instability; see Fig. 3(b).

As observed in patterning systems by both experiments [40,52,53] and simulations [54,55], final states are often found to be sensitive to the initial conditions and the size of the simulation cell. This is illustrated by Figs. 4(a) and 4(b), where a single bilayer with a large initial composition difference between the two layers can evolve into a perfect layered structure, while increasing the number of initial bilayers from 1 to 2 and/or modifying the composition contrast between initial layers can result in defective layered structures, here with "grain boundaries." Starting from solid solutions, changing the random seed for the initial composition fluctuations also produces different defective layered structures; see Figs. 4(c)
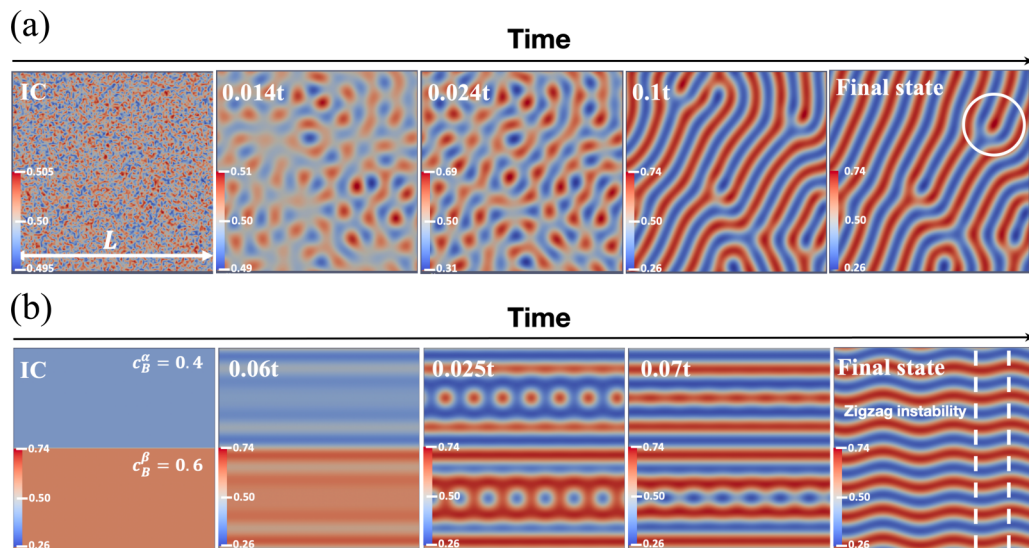

FIG. 3. Time evolution of the concentration field of an $A_{50}B_{50}$ alloy using the order-3 ECH model. α and β phases are regions in red and blue, respectively. (a) IC = solid solution with small fluctuation. Snapshots are taken at a fraction of total time t indicated at the top. A topological defect analogous to "dislocation" is encircled. (b) IC = bilayer. "Zigzag" instability marked by dashed lines.
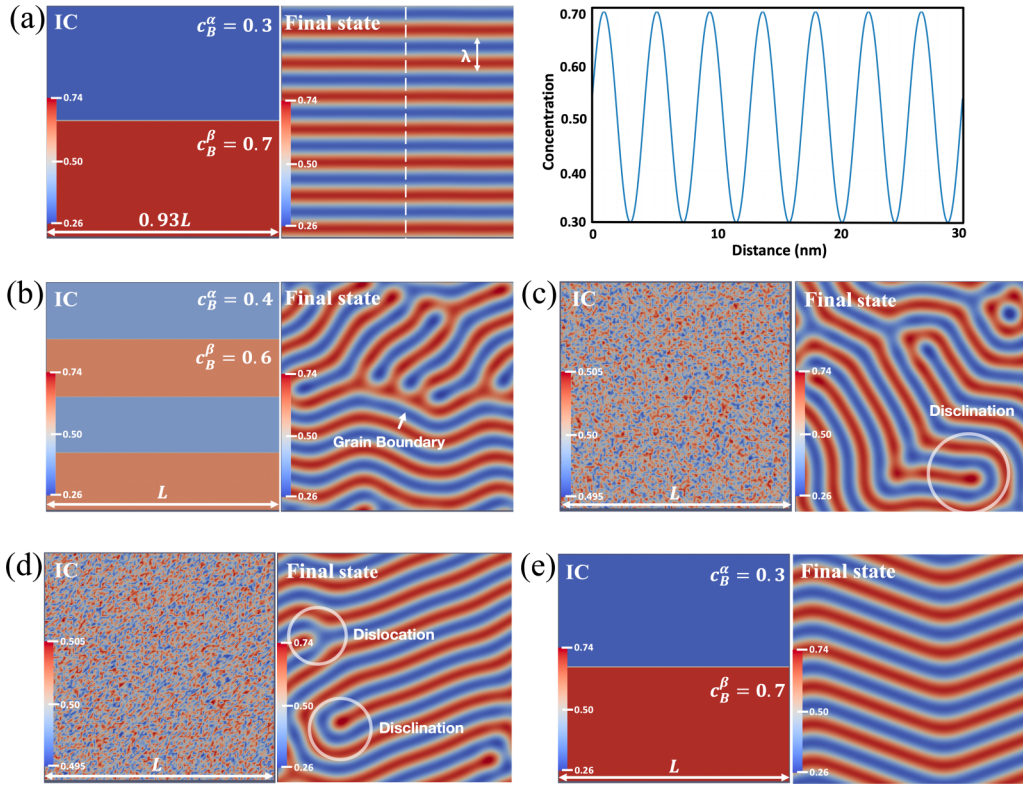
FIG. 4. Selected initial and final states with the order-3 ECH model. The final state shown in (a) is a defect-free lamellar structure with alternating phases characterized by a fixed wavelength λ. Compositional profile of B along the dashed line is shown next to the final state. (b) IC = two bilayers. A topological defect analogous to "grain boundary" separating two domains of different orientations is marked. (c),(d) IC = solid solution. "Disclinations" are encircled in the final state. (e) Same IC as (a) but in a larger domain.

and 4(d). In addition, changing the dimensions of the simulation cell can also affect the final state [see Fig. 4(e)], which has the same IC as in Fig. 4(a) but a larger simulation cell dimension that leads to a zigzag instability. The exact details of the final state are, of course, also affected by the numerical tolerance used in the simulations to define convergence (see Appendix B). The diversity of layered morphologies depicted above thus points to the fact that there exist many metastable structures in the patterning regime and that the system can be trapped in any of those structures since the evolution equation used here is deterministic.

To determine the true steady state under specific irradiation conditions, we compute the density of effective free energy F_{eff}/A [using Eq. (19), A is the area of simulation domain]. The minimum in the effective free-energy density is found to correspond to a system with periodically aligned straight stripes, which, as shown in Fig. 4(a), are characterized by a uniform wavelength. We set this state as the reference state $f_{\text{eff}}^{\text{ref}}$ and report relative free-energy densities

$f_{\text{eff}}^{\text{CP}} = F_{\text{eff}}/A - f_{\text{eff}}^{\text{ref}}$ for other defective metastable states. The values of $f_{\text{eff}}^{\text{CP}}$ of metastable states shown in Figs. 3 and 4 are listed in Table II. The effective free-energy penalty is observed to increase as more defects/sources of inhomogeneity are present. For example, in Fig. 4(c) there is a closed circle of β phase on the upper right corner, which results in a small increase of $f_{\text{eff}}^{\text{CP}}$ compared to Fig. 4(d). A grain boundary in Fig. 4(b) causes the largest $f_{\text{eff}}^{\text{CP}}$ whereas zigzag instabilities in Figs. 3(b) and 4(e) introduce only a small energy penalty.

It is also informative to analyze the compositional profiles in these layered structures. In all cases, one finds profiles that are diffuse with no plateau regions in the middle of the layers; see, for example, the compositional profile of B in Fig. 4(a). In fact, sampling over a wide range of γ in the CP regime indicates that all compositional profiles can be well fitted by a sinusoidal function, which is characteristic of the so-called weak segregation regime. This is not surprising since we have chosen an R value close to R_c, $R = 1.1R_c$. Additional simulations for larger values of R, e.g., $R = 1.5R_c$ and $R = 2R_c$,

TABLE II. Relative effective free energy density $f_{\text{eff}}^{\text{CP}}$ of defective final states in Figs. 3 and 4 compared to the perfect lamellar structure in Fig. 4(a), which is set to be the reference state.

Type of ICs	IC = MPS				IC = SS	
	Fig. 4(a)	Fig. 4(b)	Fig. 3(b)	Fig. 4(e)	Fig. 4(c)	Fig. 4(d)
$f_{\text{eff}}^{\text{CP}}$ (J/nm^2/mol)	0	0.69 ± 0.006	0.23 ± 0.004	0.10 ± 0.002	0.44 ± 0.001	0.27 ± 0.004

however, indicate that the order-3 ECH model only generates patterns belonging to the weak segregation regime. This point will be considered in more detail in Sec. V.

D. Effective interfacial energy

While effective free energies and chemical potentials were introduced in a straightforward manner in Sec. III A, the existence of a patterning regime calls for a different approach when defining an effective interfacial energy. Let us consider first the case of systems in which macroscopic phases coexist, starting with systems at thermodynamic equilibrium. The standard thermodynamics approach defines the interfacial energy as an excess quantity [45,56] since the energy penalty introduced by the presence of one isolated interface vanishes in the thermodynamic limit. In this classical analysis, A is the interfacial area, σ is the interfacial free energy (unit is energy per unit area), and $\sigma = (\frac{\partial G^{\rm exc}}{\partial A})_{T,P,N}$, where $G^{\rm exc}$ is the Gibbs free-energy difference between an infinite physical system with a planar interface and that of a hypothetical system comprised of two semi-infinite phases with compositions set by the bulk phase diagram. In a two-phase binary alloy A_xB_{1-x} described within a Cahn-Hilliard model, the interfacial free energy takes the following expression [45]:

$$\int_S \sigma dA = \int_V \left[f(c) + \frac{\kappa}{2}|\nabla c|^2 - c\mu_B^e - (1-c)\mu_A^e \right] dV. \tag{23a}$$

μ_A^e and μ_B^e are the equilibrium chemical potential of A and B species. Considering now a system with a constant cross-section A and variable length L, containing one planar interface parallel to A, the above equation can be rewritten as

$$\sigma A = AL \times \frac{1}{V} \int_V \left[f(c) + \frac{\kappa}{2}|\nabla c|^2 - c\mu_B^e - (1-c)\mu_A^e \right] dV. \tag{23b}$$

We then introduce an excess free-energy density $f^{\rm exc}$ as

$$\begin{aligned} f^{\rm exc} &= \frac{1}{V} \int_V \left[f(c) + \frac{\kappa}{2}|\nabla c|^2 - c\mu_B^e - (1-c)\mu_A^e \right] dV \\ &= \frac{1}{V} \int_V \kappa |\nabla c|^2 dV, \end{aligned} \tag{23c}$$

where the last equality derives from the stationarity of the interface [45]. Combining Eqs. (23b) and (23c), one obtains

$$f^{\rm exc} = \frac{1}{L}\sigma. \tag{23d}$$

The interfacial energy can thus be simply determined from PF simulations by calculating $f^{\rm exc}$ for systems of increasing lengths L and using the expression

$$\sigma = \lim_{L\to\infty} L f^{\rm exc}. \tag{23e}$$

With the parameters used in the present PF model, one finds that at $T = 700$ K, $\sigma V_m = 577$ J nm/mol, where V_m is the molar volume for 3D simulations, or the molar area for 2D simulations.

We can extend the above approach to the order-3 ECH model. Following an analysis of the sharp interface limit of an extended Cahn-Hilliard equation [57–59] (see also Appendix

C), the effective excess free-energy density $f_{\rm eff}^{\rm exc}$ and the effective interfacial energy $\sigma_{\rm eff}$ are now given by

$$f_{\rm eff}^{\rm exc} = \frac{1}{V} \int_V \left(\kappa_1^{\rm eff}|\nabla c|^2 + 2\kappa_2^{\rm eff}|\nabla^2 c|^2 \right) dV, \tag{24a}$$

$$\sigma_{\rm eff} = \lim_{L\to\infty} L f_{\rm eff}^{\rm exc}. \tag{24b}$$

Equations (23) and (24) have been used to calculate the effective interfacial energy in order-1, -2, and -3 ECH models, using the compositional profiles obtained from PF simulations of microstructures with planar interfaces, concentrating first on values of γ and R for which $\kappa_1^{\rm eff}$ remains positive. The patterning case will be studied in the last part of this section. Figures 5(a)–5(c) display $\sigma_{\rm eff}$ as a function of γ for the above three ECH models, normalizing $\sigma_{\rm eff}$ by the thermal equilibrium value $\sigma_{\rm th}$ at the same temperature, and normalizing γ by $\gamma_1^{\rm linear}$ for the R value used here. As we can see from the plots, $\sigma_{\rm eff}/\sigma_{\rm th}$ decreases for all three cases as γ increases. In the order-1 model, phase coexistence under irradiation can be described by an effective interaction term $\Omega_{\rm eff} = \Omega - \gamma R^2/12$, see Eq. (16), and $\sigma_{\rm eff}/\sigma_{\rm th} \to 0$ as $\gamma/\gamma_1^{\rm linear} \to 1$ since the latter limit imposes that $T/T_c^{\rm eff} \to 1$; furthermore, the reduction in $\sigma_{\rm eff}/\sigma_{\rm th}$ as $T/T_c^{\rm eff}$ increases is the one expected for a regular solution model; see, for instance, Fig. 3 in Ref. [45]. It is also of interest to extend this interfacial energy analysis in the MPS regime to the order-2 model, even though that model does not provide a physically correct behavior in the patterning regime. In the order-2 model, phase coexistence under irradiation involves an effective interaction term $\Omega_{\rm eff}$ and an effective gradient energy coefficient, $\kappa_1^{\rm eff}$, see Eq. (17), which is reduced as γ increases. As a result, the interfacial energy decreases faster than in the order-1 model, and $\sigma_{\rm eff}/\sigma_{\rm th} \to 0$ when $\kappa_1^{\rm eff} \to 0$ as seen from Eq. (17). In the order-3 model [Fig. 5(c)], the reduction rate of $\sigma_{\rm eff}/\sigma_{\rm th}$ is intermediate between the previous two cases because of a positive compensation from $2\kappa_2^{\rm eff}|\nabla^2 c|^2$. Notice that the PF simulations yielded compositional patterning for $\gamma < \gamma_1^{\rm linear}$, and the transition to patterning takes place at a small but nonzero positive interfacial energy (see the inset). This is expected as the transition from MPS to CP is a first-order transition, but weakly first-order here as the system is very close to the critical point (γ_c, R_c). The interfacial energy then gradually decreases to negative values, before increasing again to zero when the system enters the solid solution regime. The validity of $\sigma_{\rm eff}$ given by Eq. (24) is, however, problematic in the patterning regime, as discussed next.

In contrast to systems at thermodynamic equilibrium where macroscopic phases coexist, the interfacial area is an extensive quantity in the CP regime since this area scales with the volume of the system, and therefore one cannot define the interfacial free energy as an excess quantity. Furthermore, that approach may be flawed due to the absence of the well-defined bulk, or far-field, concentration values needed to describe the hypothetical system with a dividing surface used as a reference [60]. In the present work, for instance, all compositional profiles generated by the order-3 ECH model in the patterning regime have a sinewave-like shape, see Fig. 4(a), and it is found that the compositions at the minima and maxima are not independent from the period of the layered microstructures, so these extrema values cannot serve as proxies for far-field solutions.
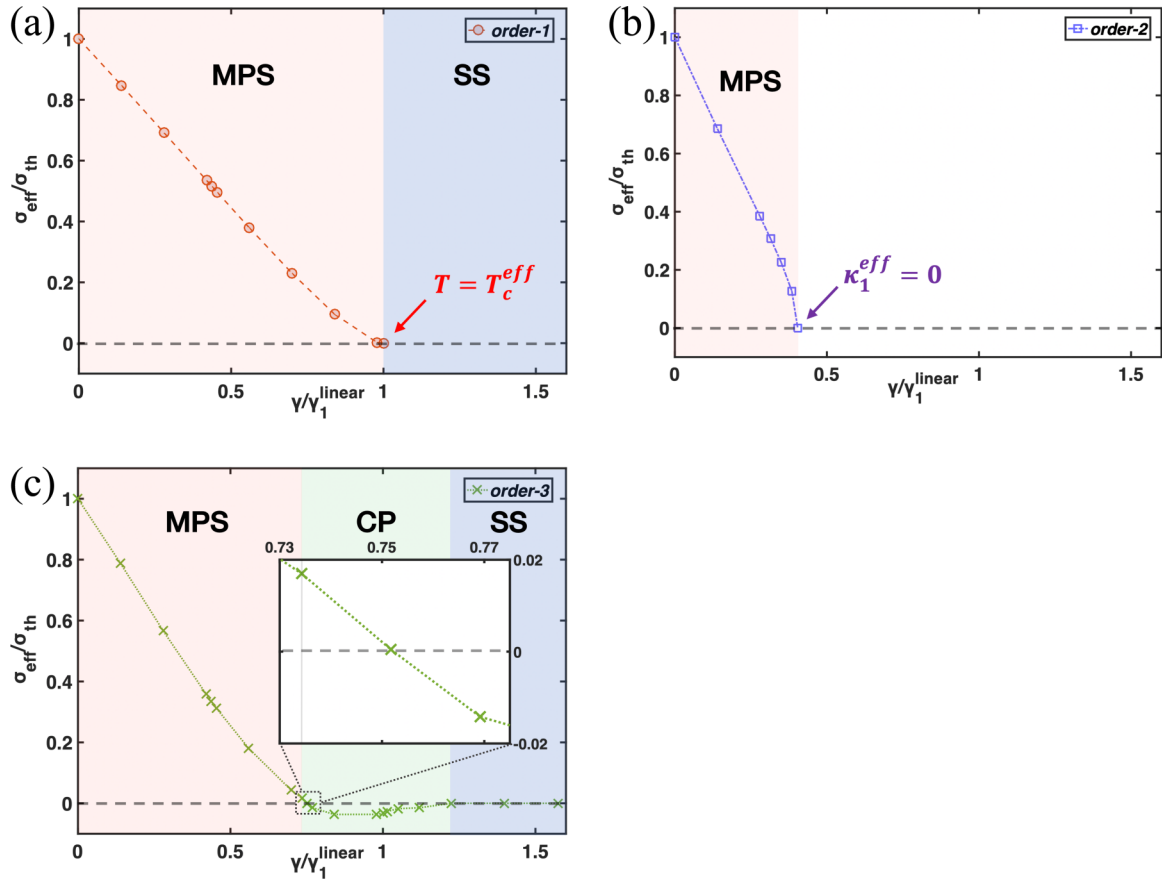
FIG. 5. The relationship between $\sigma_{\text{eff}}/\sigma_{\text{th}}$ and $\gamma / \gamma_1^{\text{linear}}$ in order-1, -2, and -3 ECH models. Random mixing decreases interfacial energy in all three cases. (a) Results of the order-1 model. σ_{eff} approaches zero at the effective critical temperature T_c^{eff}. (b) The order-2 model. σ_{eff} approaches zero when κ_1^{eff} becomes zero. (c) The order-3 model. Steady state enters the CP regime when σ_{eff} becomes a small positive value; see the inset for a magnified view of the transition region.

A modified approach is thus proposed, where we consider the dependence of the effective free-energy density with the period of layered structures. Specifically, we employ small simulation cells of constant cross section A and of variable length λ, which is chosen to be close to the periods of layered structures observed in large-cell simulations for the considered values of γ and R; see, for instance, Fig. 4(a). These small simulation cells were initialized with one straight bilayer and evolved to reach steady state. A small cross section was used so as to prevent any interface instability of the straight interface, and λ was varied only around an estimated optimum period so that no additional bilayer would nucleate, i.e., to suppress an Eckhaus instability. The effective free-energy density was measured at steady state by normalizing the total effective free energy F_{eff} defined by Eq. (19) by the area (or volume in 3D) of the simulation cells, i.e., F_{eff}/A. The relative effective free-energy density $f_{\text{eff}}^{\text{CP}}$, defined previously in Sec. III C, was observed to display a near parabolic dependence with $1/\lambda$, see for instance Fig. 6, reaching a minimum at $1/\lambda_c$. We propose to define the effective interfacial free energy in the CP regime as

$$\sigma_{\text{eff}}^{\text{CP}} = \frac{\partial f_{\text{eff}}^{\text{CP}}}{\partial (1/\lambda)}. \qquad (25)$$

While Eq. (25) bears some similarity with the definition used in the MPS regime, see Eqs. (23d) and (23e), we stress that $f_{\text{eff}}^{\text{CP}}$ is not an excess quantity in the thermodynamic sense.
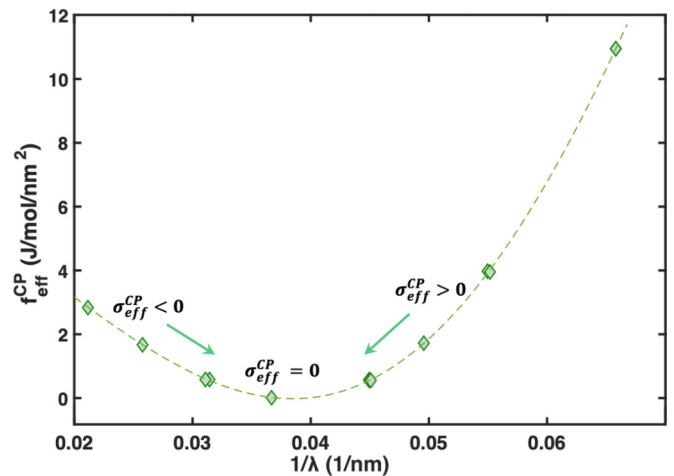

FIG. 6. Relative effective free-energy density $f_{\text{eff}}^{\text{CP}}$ vs $1/\lambda$ in WSR of patterning with the order-3 ECH model. The true steady state of CP has the lowest $f_{\text{eff}}^{\text{CP}}$ and null σ_{eff}.

Furthermore, a consequence of this definition is that the most stable periodic layered structure is the one for which $\sigma_{\text{eff}}^{\text{CP}} = 0$. When $1/\lambda$ is smaller (larger) than $1/\lambda_c$, the effective interfacial energy is negative (positive), capturing the fact that the system can lower its total effective free energy by increasing $1/\lambda$ (decreasing $1/\lambda$).

The near parabolic shape of the plot of $f_{\text{eff}}^{\text{CP}}$ versus $1/\lambda$ in Fig. 6 can be rationalized by considering the fact that in the weak segregation regime, steady-state compositional profiles are near sine-wave functions. It is proposed that stretching or compressing the patterned structure by $\pm d\lambda$ results in a similar increase of the effective free-energy density, and thus a symmetric plot for $f_{\text{eff}}^{\text{CP}}(\frac{1}{\lambda})$ near its minimum. This rationalization was tested by deriving an analytical expression of $f_{\text{eff}}^{\text{CP}}(\frac{1}{\lambda})$ using a one-mode approximation, i.e., assuming that the compositional profiles are sine waves of amplitude a and wave vector k. One modification, however, had to be made to the order-3 ECH model for deriving such an expression: The regular solution free-energy density, $f(c)$, had to be replaced by a Landau free energy as in previous analytical works [32,35], since the logarithmic terms in the configurational entropy in $f(c)$ preclude the derivation of explicit analytical expressions. As shown in Appendix D, one then obtains the following expression for $f_{\text{eff}}^{\text{CP}}(k)$:

$$\frac{f_{\text{eff}}^{\text{CP}}}{a^2} = \frac{\kappa_2^{\text{eff}}}{4}\left(k^2 - k_c^2\right)^2, \tag{26a}$$

$$k_c^2 = -\frac{\kappa_1^{\text{eff}}}{2\kappa_2^{\text{eff}}}. \tag{26b}$$

Clearly, between $f_{\text{eff}}^{\text{CP}}$ and k^2 there exhibits a parabolic relationship that scales with the square of amplitude. At k_c, the effective free-energy density reaches the minimum. As expected, the effective free-energy expression in k-space for the order-3 ECH model in the patterning regime, Eq. (26), is identical to that expected for the corresponding one-mode SH model [59].

IV. COMPOSITIONAL PATTERNING AWAY FROM THE CRITICAL POINT

PF simulations are next employed to investigate the steady states of patterning further away from the critical point (γ_c, R_c). As we will show, this requires higher order-n ECH models.

A. Convergence of the order-n ECH models with increasingly higher order

We consider here the effect of the number of inhomogeneity terms on the steady-state phase diagram. It will be shown that the further away from the critical point (γ_c, R_c), the slower is the convergence. We first investigate the question of convergence of the order-n ECH model using a linear stability analysis, before employing PF simulations.

A stability phase diagram is first built in the R-γ space through linear stability analysis of the full dispersion relation [see the full model, see Eq. (3)] and the dispersion relation of the order-n model [see Eq. (11)]. The γ_1^{linear} boundary and critical point are the same for both the full model and the order-n model since they are determined by the same equation, so only
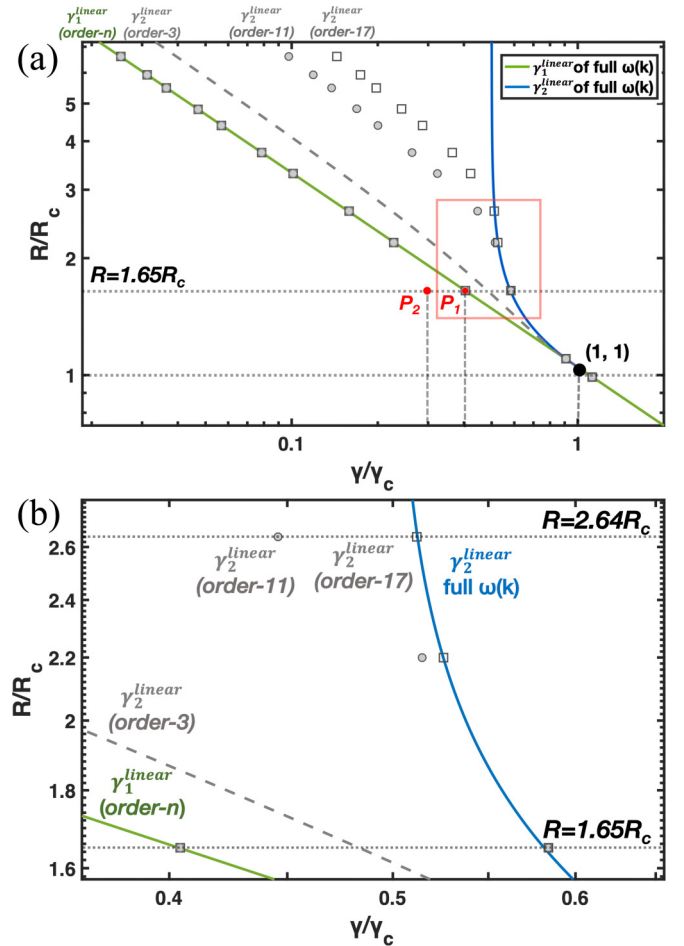

FIG. 7. (a) Boundary parameters of the order-n ECH model and the full model (marked by solid lines) in a steady-state phase diagram obtained by linear stability analysis. γ_1^{linear} is the same for all models, but $\gamma_{2-\text{order-}n}^{\text{linear}}$ deviates a lot from $\gamma_{2-\text{full model}}^{\text{linear}}$. (b) A zoom-in view of the rectangular region marked in (a).

γ_2^{linear} needs to be determined. The analytical expression of γ_2^{linear} of the full model is collected in Appendix A; for γ_2^{linear} of the order-n model, there is no simple analytical expression, so we resort to numerical methods. The resulting phase diagram is shown in Fig. 7(a). It is seen that the order-3 model matches the full model only very close to the critical point. When R becomes larger, higher-order models are required, as illustrated with order-11 and order-17 models in Figs. 7(a) and 7(b).

We then use PF simulations to study the effect of order-n on steady-state microstructures in the patterning regime by investigating the effective free-energy density, characteristic wavelength λ, and concentration profile. We conclude that convergence has been achieved when the above three measures remain essentially unchanged upon further increasing n. Similar to what was reported in Sec. III D, we use a bilayer structure as the initial condition, and we systematically change the width of the bilayer as a way to change the steady-state wavelength λ. We compare different order-n models of $R = 1.65R_c$ for γ values covering the entire range of the CP regime, but for simplicity we discuss below the simulation
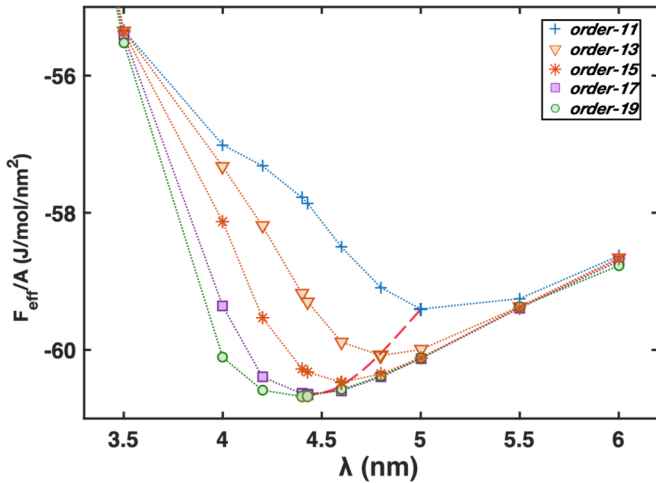
FIG. 8. The relationships between F_{eff}/A and λ of order-$n(n = 11, 13, 15, 17, 19)$ ECH models, using operating point P_2 in Fig. 7(a). The red dashed line connects the set of minima of F_{eff}/A from these order-n models. The minimum of F_{eff}/A and λ_c converge to fixed values for $n = 17$.
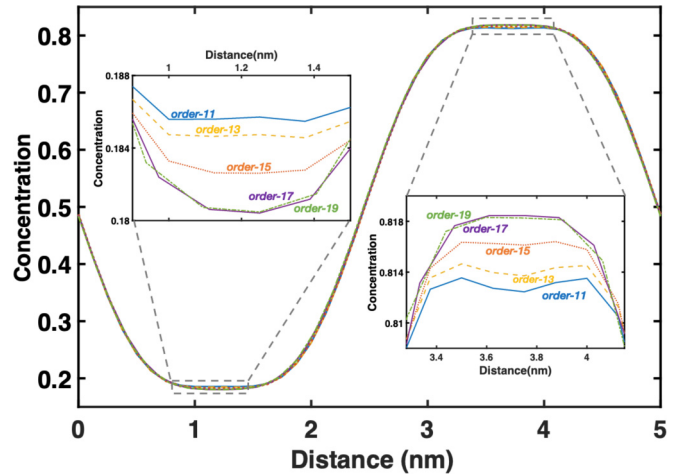

FIG. 9. Line profiles of species B across one period of patterning in order-$n(n = 11, 13, 15, 17, 19)$ ECH models, using operating point P_2 in Fig. 7(a). Insets are magnified views of the interior of each phase, showing that convergence of the steady-state profiles occurs at $n = 17$.

results obtained for one representative point, corresponding to a value of γ_{P2}; see point P_2 in Fig. 7(a).

The relationships between effective free-energy density F_{eff}/A and λ from order-$n(n = 11, 13, 15, 17, 19)$ ECH models are shown in Fig. 8. All curves are somewhat U-shaped, indicating that F_{eff}/A of each order-n model reaches a global minimum at a different critical wavelength λ_c. While all these models agree well with each other at both ends of the range of λ values considered here ($\lambda = 3.5$ or 5.5 nm), these curves deviate significantly in the central region ($3.5 < \lambda < 5.5$ nm). As n increases, both the minimum of F_{eff}/A and λ_c shift to smaller values until a saturation point is reached at $\lambda_c = 4.43$ nm. From model order-15 to order-17, λ_c is reduced by 3.8%; from 4.6 to 4.43 nm, the minimum of F_{eff}/A is reduced by 0.28%. From order-17 to order-19, there is no change in λ_c and the minimum of F_{eff}/A is reduced by only 0.047%. We therefore conclude that convergence for the minimum of F_{eff}/A and λ_c requires an order-17 model for $R = 1.65R_c$.

In addition, the steady-state microstructures of patterning in order-n models are examined, and the corresponding line profiles of species B along one period of patterning are compared in Fig. 9. All profiles belong to the strong segregation regime (SSR) of patterning as there are plateau regions within α and β phases. In agreement with the results shown for the minimum of F_{eff}/A and λ_c, the steady-state compositional profiles evolve until order-17, and they remain unchanged upon further addition of higher-order terms. This can be rationalized by noting that in the strong segregation regime, higher frequencies are required to accurately reproduce square-wave shaped profiles. Despite the fairly large number of inhomogeneity terms in these high order-n ECH models, FEM solvers are found to be very effective in solving the corresponding weak form of the phase-field equations. For instance, the computational time to reach steady state with the order-19 model is only ≈ 3 times that of the order-3 model at point P_2.

Based on the analysis and the results above, we build the full dynamical phase diagram, which includes four possible steady states, namely MPS, SSR of CP, WSR of CP, and SS as γ is increased; see Fig. 10. The kinetic evolutions of the system under various irradiation conditions are presented in Fig. S1 of the supplemental material [50]. In contrast to results on patterning near the critical point (γ_c, R_c) presented in Sec. III, the main difference is the presence of a strong segregation regime of patterning. The order-3 ECH model, or equivalently kinetic models driven by a one-mode SH free-energy functional, fails to produce this patterning regime. This point will be considered further in Sec. V.

Another interesting observation is the evolution of interfacial width as a function of γ and thus as the system transitions through different steady states. We used the 10–90 % criterion
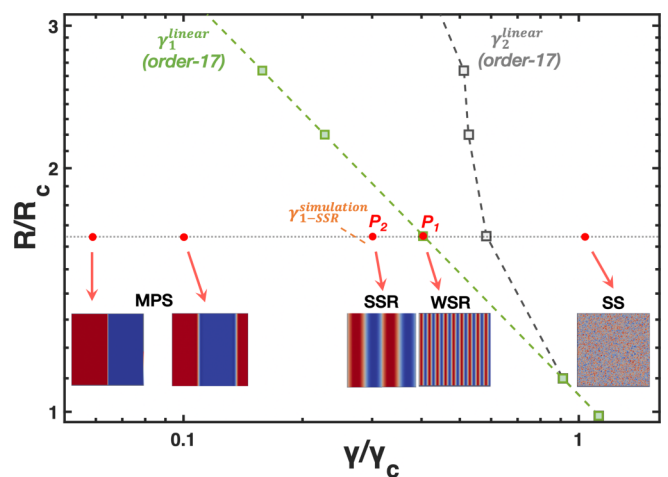

FIG. 10. Steady-state phase diagram of an irradiated $A_{50}B_{50}$ alloy. Five selected irradiation conditions at $R = 1.65R_c$ are marked by dots and connected to their steady-state microstructures. Color is rescaled based on the solubility range in each steady state.
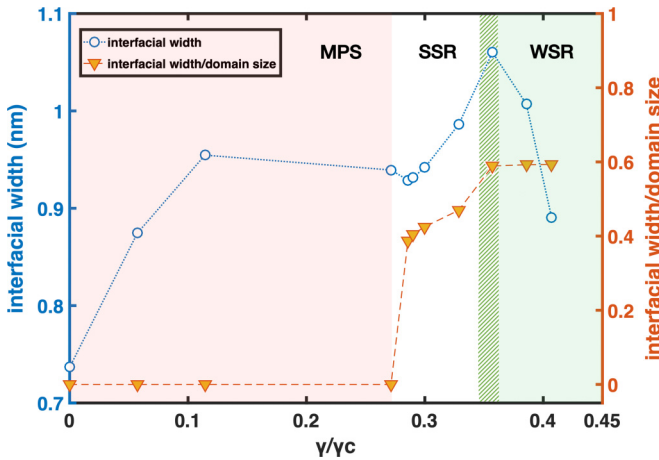
FIG. 11. Interfacial width of steady-state microstructures (MPS and CP) as a function of forcing parameter γ by an order-17 ECH model at $R = 1.65R_c$. The ratio between interfacial width and domain size is plotted to the right. Note that unlike the discontinuous transition from MPS to SSR, the change from SSR to WSR is a gradual one, and thus this gradual change is represented here by a dashed zone.

to determine the interfacial width, and we plotted its relationship with normalized γ in Fig. 11. We also measured the steady-state domain size—the distance between the center of neighboring α and β phases, and we plotted the ratio of interfacial width to the domain size as a function of γ in Fig. 11 as well. In the MPS regime, as γ increases, the interface becomes more diffuse but the ratio of interfacial width to domain size remains zero because the domain size is infinite in this regime. In SSR, larger γ leads to a substantial increase in both the interfacial width and the ratio. Entering WSR, however, the interfacial width starts to decrease as γ increases. And since the compositional profile in WSR is approximately a sine wave, the ratio of interfacial width to domain size should stay very close to a constant, ~0.5903 for a sine wave. Indeed, the last three data points shown in Fig. 11 correspond to values of 0.5889, 0.5924, and 0.5934, respectively. We thus propose that the interfacial width over domain size ratio can be used to distinguish experimentally the weak and the strong segregation regimes. This point is further discussed in Sec. V.

B. Dependence of effective interfacial energy with γ in patterning regime

We next extend the results presented in Sec. III D for the effective interfacial energy in the patterning regime with the order-3 ECH model. It is found that in the strong segregation regime, the dependence of $f_{\text{eff}}^{\text{CP}}$ with $1/\lambda$ around $1/\lambda_c$ becomes asymmetric, see Fig. 12, in contrast to the symmetric behavior measured in the weak segregation regime (Fig. 6), as well as derived analytically [Eqs. (26a) and (26b)]. Specifically, we present in Fig. 12 results from an order-17 ECH model for $R = 1.65R_c$, and four γ values at points P_2, P_3, P_4, and P_5; see Fig. 12(a). Since P_1 is in the WSR regime, the plot of $f_{\text{eff}}^{\text{CP}}$ versus $1/\lambda$ is similar to that in Fig. 6 for the order-3 ECH model, so it is not discussed further. Decreasing γ to P_2, which brings the system into the SSR regime, the shape of

the plot has become asymmetric around $1/\lambda_c$; see Fig. 12(b). For $1/\lambda < 1/\lambda_c$, the absolute value of the gradient is smaller than for $1/\lambda > 1/\lambda_c$, indicating that $f_{\text{eff}}^{\text{CP}}$ is less sensitive to the change in λ. Upon further decreasing γ to points P_3 and P_4, which are well within the SSR regime, the plots become even more asymmetric; see Figs. 12(c) and 12(d). For point P_5, which is in the MPS regime, the curve does not display a U-shape; instead, the effective free-energy density increases monotonically as $1/\lambda$ increases. These results can be rationalized considering the following points: First in the MPS regime, i.e., at P_5, Eq. (24b) predicts that in the limit of infinitely small $1/\lambda$ (or $1/L$), the slope of effective free-energy density versus $1/\lambda$ approaches σ_{eff}, and should thus be positive, since $f_{\text{eff}}^{\text{exc}}$ is related to effective free-energy density through

$$
\begin{aligned}
f_{\text{eff}}^{\text{exc}} = \frac{1}{V} \int_V & \left[f_{\text{bulk}}^{\text{eff}}(c) + \kappa_1^{\text{eff}} |\nabla c|^2 + 2\kappa_2^{\text{eff}} |\nabla^2 c|^2 \right. \\
& \left. - c\mu_B^{\text{eff}} - (1-c)\mu_A^{\text{eff}} \right] dV \\
= & F_{\text{eff}}/A - \mu_B^{\text{eff}}.
\end{aligned}
\tag{27}
$$

The slope measured at point P_5, 24.3 J nm/mol, is indeed in good agreement with the value measured from Eq. (24b), 22.5 J nm/mol. Second, in the SSR, since the compositional profiles reach plateau values within each phase, see Fig. 9, it is expected that, when interfaces are farther apart from each other than the optimum distance $\lambda_c/2$, the corresponding increase in effective free energy should be much smaller than the increase brought about by overlapping interface profiles in the case $1/\lambda > 1/\lambda_c$, and therefore that the plot of $f_{\text{eff}}^{\text{CP}}$ versus $1/\lambda$ should no longer be symmetric.

V. DISCUSSION

In this work, we have calculated the evolution of the concentration field $c(\mathbf{r}, t)$ in a phase-separating binary alloy subjected to irradiation where forced atomic replacements are described by an athermal Gaussian mixing term. For most irradiation collisions, the characteristic length of these forced displacements, R, extends beyond that of thermal diffusion, i.e., one nearest-neighbor atomic distance. This separation of length scales makes it difficult to derive an exact explicit expression of the effective potential governing the overall evolution of this system with two competing dynamics. This issue has usually been addressed by relying on approximations involving linearization of the thermodynamic free-energy density either in reciprocal space [32] or in real space [36]. In this work, we have proposed a different approach: Using an expansion of the forced mixing kinetics, finite-range mixing is expressed by a series of derivatives of $c(\mathbf{r}, t)$ evaluated at position $\mathbf{r}$, instead of evaluations of $c(\mathbf{r}', t)$ at positions $\mathbf{r}'$ far from $\mathbf{r}$. Truncating this expansion yields a series of approximate mixing models; see Eq. (6). These differential terms can then be directly incorporated into the Cahn-Hilliard evolution equation used for the thermodynamics-controlled dynamics, yielding a series of extended Cahn-Hilliard (ECH) models [see Eq. (10)] referred to order-n ECH models. As a result, for each of these order-n ECH models, exact expressions for the corresponding effective free energies were
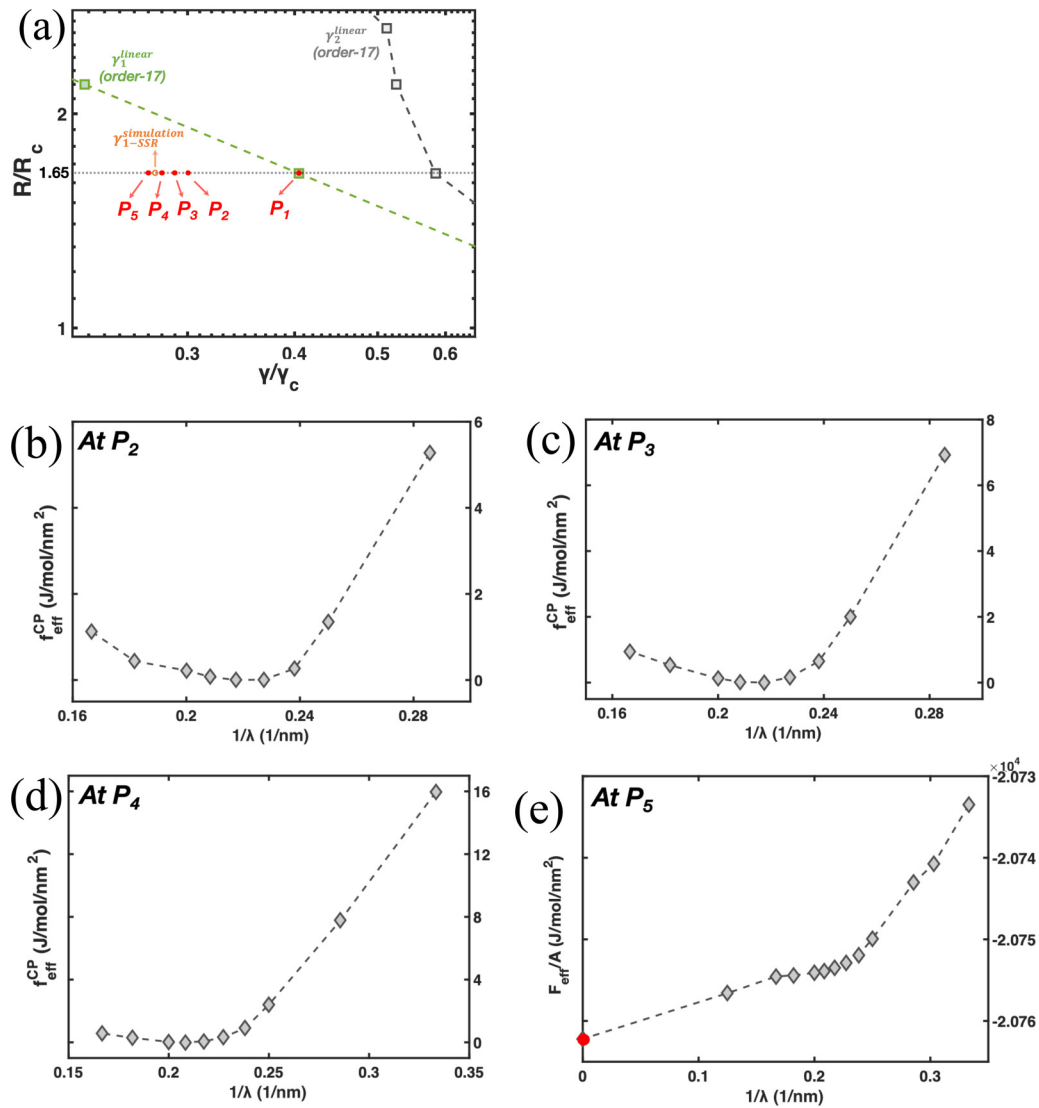
FIG. 12. (a) Steady-state phase diagram highlighting five operating points: P_1 (WSR), P_2 (SSR), P_3 (SSR), P_4 (very close to the border of SSR and MPS), and P_5 (MPS). Using the order-17 ECH model, plot of relative effective free-energy density $f_{\text{eff}}^{\text{CP}}$ vs $1/\lambda$ in the patterning regime in (b) at P_2, (c) at P_3, and (d) at P_4, respectively. (e) Effective free energy density as $1/\lambda$ for P_5 in the MPS regime.

obtained; see Eq. (13). In contrast to past works, our approach yields a unique explicit real-space expression of the effective free energy for all three steady-state regimes. Steady-state concentration profiles were then calculated using phase-field simulations, see Figs. 4 and 9, and used to build steady-state phase diagrams, see Figs. 7 and 10. It was found that an order-3 model is sufficient to capture the onset of patterning, where concentration profiles are close to sine waves, i.e., in the weak segregation regime. Higher-order models, however, were required to generate the strong segregation regime expected deep into the patterning regime, as illustrated in Fig. 9. We specifically discuss in this section two key points: (i) the definition of an effective interfacial free energy in the above driven alloy system, and (ii) the connection between the present effective free energies with those obtained in previous models of alloys under irradiation, and more broadly of systems undergoing patterning.

Defining an effective interfacial free energy for systems that display a transition between steady states of macroscopic

phase separation and compositional patterning is problematic. In the MPS steady state, i.e., at low forcing intensity γ, one can extend the standard thermodynamic approach to calculate the interfacial free energy by simply using the effective free energy defined in Eq. (19). The resulting effective interfacial energy σ_{eff}, defined through Eq. (24b), is found to decrease as γ increases and to reach negative values for γ values nearly equal to the one corresponding to the transition to CP; see Fig. 5(c). The fact that the patterning regime can be associated with a negative interfacial energy may not be too surprising at first since an initially macroscopic system operating in that regime will spontaneously create new interfaces until reaching the optimum lamellar structure. Negative interfacial energies have been used or calculated in other systems self-organizing into mesoscopic patterns, for instance in active matter [38,39], although this topic remains controversial [61]. This definition for the effective interfacial energy, however, cannot be used in the present patterning regime. First, the interfacial area is no longer an excess quantity. Instead, in the patterning

regime, the interfacial area scales with the volume, i.e., it is now an extensive quantity. Second, the steady-state compositional profile does not admit constant "far-field" solutions as the interface width and phase coexistence length scale are no longer decoupled. For the nearly sinewave concentration profiles found in the weak segregation regime, for instance, these two scales are identical, up to a factor 2. In contrast, the existence of far-field solutions that are constant over distances much larger than that of the interface width is an essential requirement for the derivation of interfacial free energy from phase field models using a sharp interface limit; see, for instance, Refs. [57,62] and Appendix C.

We thus introduced in this work an alternative definition of the effective interfacial energy in the CP regime, $\sigma_{\text{eff}}^{\text{CP}}$. Since the patterning period λ is an internal degree of freedom of the system, an effective interfacial energy should be related to the dependence of the effective free-energy density with respect to that period. Specifically, we define $\sigma_{\text{eff}}^{\text{CP}}$ as the partial derivative of the effective free-energy density with respect to $1/\lambda$, see Eq. (25), so that $\sigma_{\text{eff}}^{\text{CP}}$ is properly dimensioned, i.e., in energy units per $(L)^{(d-1)}$, where L is a system length and d is the system spatial dimension. We find that the effective free-energy density of a steady-state lamellar phase varies continuously with its period λ, see Fig. 6, thus ensuring that this partial derivative is well-defined for the systems of interest here. An important consequence of this definition is that $\sigma_{\text{eff}}^{\text{CP}} = 0$ for the most stable lamellar steady state. This approach is in fact consistent with other approaches used to study related systems. For example, we already noted in Sec. III that the order-3 ECH free energy is very similar to the functional form used in some phase-field crystal (PFC) models [63,64]. Atoms in PFC simulations correspond to spherical precipitates in our work, and equilibrium PFC states with crystalline order correspond to a patterning regime with periodic structures. Figure 6 is thus the counterpart of a plot of the system energy per atom as a function of inverse lattice parameter in PFC. This suggests that the curvature $\partial^2 f_{\text{eff}}^{\text{CP}} / \partial (1/\lambda)^2$ evaluated at $\sigma_{\text{eff}}^{\text{CP}} = 0$, defining an effective "interfacial modulus," could be used to characterize the compliance of the lamellar phase in response to changing its wavelength. Another correspondence can be made with the concept of defactant introduced by Kirchheim [65,66] and used in particular to rationalize the stabilization of nanocrystalline materials to a finite grain size by doping grain boundaries with suitable solute atoms. Although there is no direct model correspondence here, in part because including grains of distinct crystallographic orientations in phase-field modeling requires the addition of nonconserved order parameters, Kirchheim reaches a similar conclusion, i.e., that the effective grain boundary energy should be zero for the most stable nanocrystalline state.

We next turn to the effective free-energy potentials derived from order-n models and to their comparisons with potentials obtained in previous publications on systems undergoing patterning, in particular alloys under irradiation. As noted above, in the compositional patterning regime, our order-3 effective free energy, see Eq. (19), is equivalent to the one-mode SH potential [3,59] since $\kappa_1^{\text{eff}} < 0$ in that regime [note that Eq. (19) differs slightly from the standard one-mode SH free energy because of the entropic terms in $f(c)$]. Such an

effective potential was recently obtained by Simeone *et al.* [36] for alloys under irradiation with an exponential-decay forced mixing, by performing a second-order expansion of the k-space response function around the dominant patterning wave vector (see Ref. [36] for details). Our order-3 effective free energy is, however, more general since it encompasses both the traditional extended CH model in the MPS regime, where the γ values are low enough that $\kappa_1^{\text{eff}} > 0$, and an SH free energy once the system enters the patterning regime, i.e., at higher γ values. It is intriguing to note that a potential analogous to the order-3 effective free energy was used to model shape instability in a static but frustrated system, where phase separation competes with dipole-dipole repulsion. One limitation of those potentials for alloys under irradiation is that they can only generate patterns that belong to the weak segregation regime. Higher-order ECH models overcome this limitation by including higher-order derivatives of the concentration field $c(\mathbf{r}, t)$. This is rationalized by considering that higher-order compositional inhomogeneity terms are able to capture higher-order harmonics, which are required to generate the square-wave-like profiles of the strong segregation regime. While we are not aware of any systematic parallel with other effective potentials for patterning under irradiation, it is interesting to note that our order-5 model is very similar to the two-mode SH potential, as detailed in Appendix D: both potentials include terms up to $|\nabla^4 c|^2$, and in both cases the signs of the coefficients of $|\nabla^n c|^2$ alternate from negative to positive for $n = 1, 2, 3, 4$ (see Appendix D for details). Such two-mode SH potentials have been employed recently for PFC models, in part to provide more flexibility and accuracy in generating crystalline phases with face-centered-cubic and close-packed-hexagonal lattices [67,68]. Extending further this comparison between the order-5 model and the two-mode SH potential, we suggest that our order-n effective potentials could be alternatively defined as multimodal SH potentials with $(n-1)/2$ patterning modes.

Next, the present work suggests that, when investigating experimentally compositional patterning, it would be useful to determine whether the system is in a weak segregation or a strong segregation regime. This would also help to determine whether experimental ballistic relocation distances can be large enough to stabilize the strong segregation regime. Existing data obtained from atom probe tomography point to fairly diffuse interfaces, typically $\approx$1–2 nm wide, in the compositional patterning regime for Fe-Cr [20–23], Cu-Fe [69], and Cu-V [70]. These observations alone are, however, not sufficient to conclude that these alloys were in the WSR, since diffuse interfaces can be found in the SSR; see Fig. 11. A conclusive test, however, is to determine the ratio of the interfacial width to the precipitate radius at steady state as a function of the forcing intensity, as shown in Fig. 11. This sequence of steady states could, for instance, be obtained by decreasing the irradiation temperature. In the WSR, this ratio is expected to remain a constant, $\sim$0.5903 for a sine wave, while in the SSR this ratio decreases continuously upon approaching the γ_1 boundary, where the ratio becomes zero in MPS regime.

Lastly, we point to potential extensions of the present work. In light of the recent steady-state phase diagram obtained by Luneville *et al.* [37], it would be interesting to use

order-n ECH models to study nonequiatomic compositions and contrast the evolution of precipitate shapes in the WSR and SSR regimes. Secondly, since deterministic evolution equations were used in this work, spatial and temporal correlation events in mixing events were not considered. These correlations could, however, be introduced by treating forced mixing events as a stochastic source term, similarly to what Dubey and El-Azab did for capturing point defect production by displacement cascades [71]. In fact, another significant extension would be to explicitly include the point defects created by irradiation, as well as the microstructural defects that serve as sinks for those point defects, e.g., grain boundaries. This extension would make it possible to include in PF simulations radiation-induced segregation and precipitation driven by the kinetic coupling of chemical and defect fluxes to sinks [72]. This is of interest because systems driven by nonzero net fluxes can undergo nonequilibrium phase transitions distinct from those with zero net fluxes [73,74].

VI. CONCLUSION

In this paper, we studied macroscopic phase separation (MPS) and compositional patterning (CP) in a binary alloy subjected to irradiation where finite-range mixing is modeled using a Gaussian distribution. Using an expansion and truncation of this Gaussian distribution to order n, we introduced a series of approximate models and were able to define exact effective potentials for each order-n model. This is in contrast to past approaches that retained an exact expression for their mixing function, but they could only obtain approximate explicit expressions for the effective potential governing the overall evolution of the alloy under irradiation. Interestingly, our lowest-order effective free energy, the order-3 one, yields a one-mode Swift-Hohenberg functional in the CP regime, in agreement with recent results by Simeone *et al.* [31] after linearization of the thermodynamic free-energy density. As the irradiation forcing intensity is reduced, the coefficient of the gradient square inhomogeneity term in this order-3 potential changes sign, from negative to positive at the transition from CP to MPS, and the effective free energy becomes an extended Cahn-Hilliard functional. The order-3 effective potential thus provides a unified description of the effective free energy for the system across the MPS and CP regimes. Phase-field simulations for equiatomic compositions in 2D systems yield regular lamellar phases at steady state in the CP regime, as expected. Simulations using the order-3 potential, however, generate only sinewave-like concentration profiles, which are characteristic of the weak segregation regime. Furthermore, analysis of the convergence of these profiles as the order n increases shows that the order-3 potential is only valid near the onset of patterning, specifically near the critical point (γ_c, R_c) of the steady-state phase diagram; see Fig. 10. Deeper into the patterning, higher-order models are required, and near the MPS-CP boundary, they produce square-wave-like profiles, characteristic of the strong segregation regime. Drawing from the two-mode SH functionals developed for phase-field crystal models, we showed that our order-n functionals are analogous to multimodal SH functionals. A second key result from this work concerns effective interfacial energies. Defining effective interfacial energies for systems in the CP steady

state requires a novel approach: In that regime, the interfacial area is no longer an excess quantity as it becomes proportional to the system's volume, i.e., an extensive quantity, thus precluding the use of the traditional approach employed for systems where macroscopic phases coexist at thermodynamic equilibrium. An alternative approach was introduced, defining the effective interfacial energy in the CP regime as the partial derivative of the effective free-energy density with respect to the inverse of the pattern period. Using this approach, the most stable lamellar steady state is one for which the effective interfacial energy is zero. It will be interesting to extend the present work to nonequiatomic compositions and 3D systems, in order to further assess the influence of the order n on steady-state microstructures and precipitate composition.

APPENDIX A: BOUNDARY PARAMETERS BY LINEAR STABILITY ANALYSIS

Derivations of important boundary parameters of steady-state regimes in the dynamical phase diagram are presented in this appendix. We use Eq. (21) in Sec. III A to derive boundary parameters for the order-3 ECH model: γ_1^{linear}, the boundary between MPS and CP regime, is corresponding to $\frac{d\omega}{dk}$ changing sign at $k = 0$, so

$$\gamma_1^{\text{linear}} = -\frac{6f''}{R^2}.$$

γ_2^{linear}, the boundary between CP and SS, is determined by $\frac{d\omega}{dk}|_{k=k_c} = 0$ and $\omega(k_c) = 0$,

$$\gamma_2^{\text{linear}} = \frac{9\kappa R^4 + f'' R^6 - \sqrt{(9\kappa R^4 + f'' R^6)^2 + 135\kappa^2 R^8}}{-\frac{5}{24}R^8}.$$

The onset of patterning (γ_c, R_c) is obtained by setting $\gamma_1^{\text{linear}} = \gamma_2^{\text{linear}}$, so we have

$$\gamma_c = \frac{(f'')^2}{2\kappa}, \quad R_c = 2\sqrt{\frac{3\kappa}{-f''}}.$$

In the patterning regime, the boundaries of the range of wave vectors with positive growth rates (k_1, k_2) are the two positive real roots of Eq. (21),

$$k_1 = \sqrt{\frac{-\kappa_1^{\text{eff}} - \sqrt{(\kappa_1^{\text{eff}})^2 - 4\kappa_2^{\text{eff}}\frac{\partial^2 f_{\text{bulk}}^{\text{eff}}}{\partial c^2}}}{2\kappa_2^{\text{eff}}}},$$

$$k_2 = \sqrt{\frac{-\kappa_1^{\text{eff}} + \sqrt{(\kappa_1^{\text{eff}})^2 - 4\kappa_2^{\text{eff}}\frac{\partial^2 f_{\text{bulk}}^{\text{eff}}}{\partial c^2}}}{2\kappa_2^{\text{eff}}}}.$$

For the patterning regime away from the critical point, in Sec. IV A, Eq. (3) is used to derive γ_2^{linear} of the full model:

$$\gamma_{2-\text{full model}}^{\text{linear}} = \frac{16\kappa^2 + \frac{(f'' R^2)^2}{9}}{\frac{4}{9}\kappa R^4}.$$

APPENDIX B: NUMERICAL METHODS

Numerical simulations of phase-field equations are obtained via an open source, massive parallel finite-element method (FEM) framework, MOOSE. The FEM scheme is fully coupled and fully implicit featured with adaptive meshing and timing. For FEM discretization, the residual equation of the partial differential equation and its variational Galerkin weak form are constructed. ψ_m is used as the test function for the weighted integral residual, and divergence theorem is applied to lower the order of the derivatives in the usual manner. Since in Eq. (10) there are many higher-order gradient terms, to avoid the use of computationally expensive higher-order basis functions for both trial and test functions, we introduce a number of intermediate variables instead to systematically represent these higher-order gradient terms. This operation can significantly improve the efficiency of solving convergence, but it does not impact the accuracy of solution. Residual equations in a split weak form are (i stands for the species of the system)

$$R_{\mu_i} = \left(\frac{\partial c_i}{\partial t}, \psi_m\right) + (M_i \nabla \mu_i, \nabla \psi_m) - \langle M_i \nabla \mu_i \cdot \overrightarrow{n}, \psi_m \rangle,$$

$$R_{c_i} = \left(\left(\frac{\partial f_{\text{bulk}}}{\partial c_i} - \mu_i\right), \psi_m\right) + (\nabla c_i, \nabla(\kappa_i \psi_m))$$
$$- \langle \nabla c_i \cdot \overrightarrow{n}, \kappa_i \psi_m \rangle.$$

The $(*,*)$ operator represents a volume integral with an inner product, and the $\langle *, * \rangle$ operator represents a surface integral with an inner product. c_i is the conserved variable and μ_i is the chemical potential. For the periodic boundary condition, boundary integral terms are neglected, so we omit the surface integrals,

$$R_{\mu_i} = \left(\frac{\partial c_i}{\partial t}, \psi_m\right) + (M_i \nabla \mu_i, \nabla \psi_m),$$

$$R_{c_i} = \left(\left(\frac{\partial f_{\text{bulk}}}{\partial c_i} - \mu_i\right), \psi_m\right) + \left(\left(\kappa_i - \frac{D_2}{M_i}\right)\nabla c_i, \nabla \psi_m\right)$$
$$+ \left(\frac{D_1}{M_i}c_i - \frac{D_1}{2M_i}, \psi_m\right) - (\nabla \alpha_i^{\text{1st}}, \nabla \psi_m),$$

$$R_{\alpha_i^{\text{1st}}} = \left(\alpha_i^{\text{1st}}, \psi_m\right) + \left(\frac{D_3}{M_i}\nabla c_i, \nabla \psi_m\right) + (\nabla \alpha_i^{\text{2nd}}, \nabla \psi_m),$$

$$R_{\alpha_i^{\text{2nd}}} = \left(\alpha_i^{\text{2nd}}, \psi_m\right) + \left(\frac{D_4}{M_i}\nabla c_i, \nabla \psi_m\right) + (\nabla \alpha_i^{\text{3rd}}, \nabla \psi_m),$$

$$\cdots$$

$$R_{\alpha_i^{(n-3)\text{th}}} = \left(\alpha_i^{(n-3)\text{th}}, \psi_m\right) + \left(\frac{D_{n-1}}{M_i}\nabla c_i, \nabla \psi_m\right)$$
$$+ (\nabla \alpha_i^{(n-2)\text{th}}, \nabla \psi_m),$$

$$R_{\alpha_i^{(n-2)\text{th}}} = \left(\alpha_i^{(n-2)\text{th}}, \psi_m\right) + \left(\frac{D_n}{M_i}\nabla c_i, \nabla \psi_m\right),$$

$$\mu_i = \frac{\partial f(c_i)}{\partial c_i} - \kappa \nabla^2 c_i + \frac{D_1}{2M_i}(2c_i - 1) + \frac{D_2}{2M_i}\nabla^2 c_i + \nabla^2 \alpha_i^{\text{1st}},$$

$$\alpha_i^{(n-3)\text{th}} = \frac{D_{n-1}}{M_i}\nabla^2 c_i + \nabla^2 \alpha_i^{(n-2)\text{th}},$$

$$\alpha_i^{(n-2)\text{th}} = \frac{D_n}{M_i}\nabla^2 c_i.$$

α_i^{1st} to $\alpha_i^{(n-2)\text{th}}$ are intermediate variables to split the higher-order equations. First-order 2D Lagrange shape functions are used for all variables, and volume integrals are discretized by setting the reference element type as four-node quadrilateral in 2D (QUAD4). The interfacial thickness (2ξ) is resolved by more than 10 grid points (much finer than the usual $2\xi = 6\Delta x$ criterion), for a good balance between computational efficiency and numerical accuracy. The method for time integration is backward Euler. The solve type for the nonlinear system is Newton's method. The method carried out to manipulate the preconditioning matrix is the additive Schwartz method (ASM), which is the only option that works well with the split Cahn-Hilliard equations, and sub-preconditioning is performed by using LU factorization. The simulations are solved with a nonlinear relative tolerance of 10^{-8} and a nonlinear absolute tolerance of 10^{-9}. Adaptive mesh refinement and timing are implemented to accommodate the large concentration variation across the interface and to reduce computational time. Parallelism by the message passing interface (MPI) is applied to all simulations, and the average degrees of freedom (DOFs) per core is targeted to be 20 000 for the best computational performance with various domain sizes.

Note that the mixing coefficient D_n in Eq. (5) has a different form if the dimension of the problem changes. For example, in two dimensions, the denominator becomes $4^p p!$, and in one dimension it is $2^p p!$. We can express the forcing parameters γ and R based on their relative distance from the critical point, so that the steady-state phase diagram is not affected by the dimension of the problem.

APPENDIX C: DERIVATION OF INTERFACIAL ENERGY BY THE SHARP INTERFACE LIMIT OF THE PF MODEL

This appendix derives interfacial energy in an order-3 ECH model from the sharp interface limit of PF models of one conserved order parameter with notations used in Refs. [57,59]. Interested readers should to read the referenced papers for a thorough understanding of the description of methods shown below.

The free-energy functional of an order-3 ECH model is expressed in the form

$$F = \int_V \left[f(c) + \frac{\kappa_1 \varepsilon^2}{2}|\nabla c|^2 + \frac{\kappa_2 \varepsilon^4}{2}|\triangle c|^2 \right]dV,$$

where c is the fractional concentration of one component in a binary system, $f(c)$ is the bulk free energy, ε is a constant that sets the scale of the interfacial energy, and κ_1 and κ_2 are coefficients of gradient and Laplacian terms. The outer expansions of field variables c, chemical potential μ, and diffusion flux **J** follow the treatment in Ref. [57], except no subscripts are needed since there are only two components in this system. A curvilinear coordinate (r,s) is used to describe the physical interface. In the inner region, the derivatives of all fields with respect to r (interface normal) are much larger than the derivatives with respect to s (interface tangent) when curvature vanishes, so a stretched variable $z = r/\varepsilon$ is introduced. The spatial and time derivatives are expressed in their transformed form accordingly. One can then express the solutions and fields of the inner and outer regions by their

asymptotic series, and a tilde is used to denote the inner expansions.

In the coarsening regime, when the driving force or the interface velocity is small, the steady-state diffusion field is allowed to form in front of the interface. The time derivative operator ∂_t can be replaced by a slow timescale, ∂_{t1}, so the outer equation is

$$\varepsilon \partial_{t1} c = -\nabla \cdot \mathbf{J}, \quad x \text{ in the outer region.}$$

For the leading order $O(1)$,

$$0 = -\nabla \cdot \mathbf{J}^0.$$

The leading-order terms of μ^0 and c^0 are close to equilibrium, so $\mu^0 = \mu_A^0 - \mu_B^0 = 0$ and $c^0 = c_{\text{eq}}^0$ for x in the outer region of the matrix and precipitate phases. For the next-to-the-leading order, $O(\varepsilon)$, we have

$$\varepsilon \partial_{t1} c_0 = -\varepsilon \nabla \cdot \mathbf{J}^1,$$

where $\mathbf{J}^1 = M^0 \nabla \mu^1 + M^1 \nabla \mu^0 = M^0 \nabla \mu^1$ since μ^0 is 0. Therefore, the first-order terms in the bulk phases are in steady state.

In the inner region, we expand the fields with t replaced by t_1 and we use κ as the mean curvature, so the Laplacian and bi-Laplacian operators in curvilinear coordinates are

$$\nabla \cdot \nabla = \frac{1}{\varepsilon^2} \partial_z^2 + \frac{1}{\varepsilon} \kappa \partial_z + \nabla_s^2,$$

$$\nabla^4 = \frac{1}{\varepsilon^4} \partial_z^4 + \frac{2}{\varepsilon^3} \kappa \partial_z^3 - \frac{1}{\varepsilon^2} \kappa^2 \partial_z^2 + \frac{1}{\varepsilon} \kappa^3 \partial_z + \nabla_s^4,$$

and

$$\widetilde{\mu^0} = f_{,\tilde{c}}(\widetilde{c^0}) - \kappa_1 \partial_z^2 \widetilde{c^0} + \kappa_2 \partial_z^4 \widetilde{c^0},$$

$$\widetilde{\mu^1} = f_{,\tilde{c}\tilde{c}}(\widetilde{c^0}) \widetilde{c^1} - \kappa_1 \partial_z^2 \widetilde{c^1} - \kappa_1 \kappa \partial_z \widetilde{c^0} + \kappa_2 \partial_z^4 \widetilde{c^1} + 2\kappa_2 \kappa \partial_z^3 \widetilde{c^0}.$$

The inner equations can be written as

$$\varepsilon^3 \partial_{t1} \tilde{c} - \varepsilon^2 \partial_{t1} r \partial_z \tilde{c} = \partial_z (\tilde{M} \partial_z \tilde{\mu}) + \varepsilon \tilde{M} \kappa \partial_z \tilde{\mu} + \varepsilon^2 \nabla_s \cdot (\tilde{M} \nabla_s \tilde{\mu}).$$

For the leading order $O(1)$, we have $\partial_z (\tilde{M} \partial_z \tilde{\mu}) = 0$, which yields $\widetilde{\mu^0} = 0$, so the same steady-state conditions are satisfied in the front as they are in the outer expansion, and $\mu^0 = 0$ applies everywhere in the domain. For the next-to-leading order $O(\varepsilon)$, recall that $\mu^0 = 0$, so we have $\partial_z (\widetilde{M^0} \partial_z \widetilde{\mu^1}) = 0$. Clearly, μ^1 is independent of z, which is the interface normal direction, so we have $\widetilde{\mu^1} = A(s, t)$. We can conclude, by matching the outer and inner expansions at $O(1)$ and $O(\varepsilon)$, that (i) $\mu^0 = 0$ everywhere in the domain (both inner and outer regions) and (ii) $\widetilde{\mu^1} = A(s, t)$.

Knowing the relation between $\widetilde{c^0}$ and c^0, and that $\widetilde{c^0}$ is the equilibrium concentration at the planar interface so its first-, second-, and higher-order derivatives at infinity have to be zero, we apply the same projection method to $\widetilde{\mu^1}$ to show

$$\int_{-\infty}^{+\infty} \widetilde{\mu^1} \partial_z \widetilde{c^0} dz$$

$$= \int_{-\infty}^{+\infty} f_{,\tilde{c}\tilde{c}}(\widetilde{c^0}) \widetilde{c^1} \partial_z \widetilde{c^0} dz - \int_{-\infty}^{+\infty} \kappa_1 \partial_z^2 \widetilde{c^1} \partial_z \widetilde{c^0} dz$$

$$- \int_{-\infty}^{+\infty} \kappa_1 \kappa \left(\partial_z \widetilde{c^0}\right)^2 dz + \int_{-\infty}^{+\infty} \kappa_2 \partial_z^4 \widetilde{c^1} \partial_z \widetilde{c^0} dz$$

$$+ \int_{-\infty}^{+\infty} 2\kappa_2 \kappa \partial_z^3 \widetilde{c^0} \partial_z \widetilde{c^0} dz.$$

The last term can be replaced by

$$\int_{-\infty}^{+\infty} 2\kappa_2 \kappa \partial_z^3 \widetilde{c^0} \partial_z \widetilde{c^0} dz$$

$$= 2\kappa_2 \kappa \left(\partial_z^2 \widetilde{c^0} \partial_z \widetilde{c^0}\right) |_{-\infty}^{+\infty} - \int_{-\infty}^{+\infty} 2\kappa_2 \kappa \left(\partial_z^2 \widetilde{c^0}\right)^2 dz$$

$$= - \int_{-\infty}^{+\infty} 2\kappa_2 \kappa \left(\partial_z^2 \widetilde{c^0}\right)^2 dz.$$

The summation of the other three κ-independent terms on the right-hand side is zero when all orders of concentration gradient terms at infinity are assumed to be zero,

$$\int_{-\infty}^{+\infty} f_{,\tilde{c}\tilde{c}}(\widetilde{c^0}) \widetilde{c^1} \partial_z \widetilde{c^0} dz$$

$$= \int_{-\infty}^{+\infty} \frac{\partial}{\partial_z} [f_{,\tilde{c}}(\widetilde{c^0})] \widetilde{c^1} dz$$

$$= f_{,\tilde{c}}(\widetilde{c^0}) \widetilde{c^1} |_{-\infty}^{+\infty} - \int_{-\infty}^{+\infty} f_{,\tilde{c}}(\widetilde{c^0}) \partial_z \widetilde{c^1} dz$$

$$= - \int_{-\infty}^{+\infty} f_{,\tilde{c}}(\widetilde{c^0}) \partial_z \widetilde{c^1} dz, \tag{C1}$$

$$- \int_{-\infty}^{+\infty} \kappa_1 \partial_z^2 \widetilde{c^1} \partial_z \widetilde{c^0} dz$$

$$= - \int_{-\infty}^{+\infty} \kappa_1 \partial_z \widetilde{c^0} \frac{\partial}{\partial_z} (\partial_z \widetilde{c^1}) dz$$

$$= - \kappa_1 \partial_z \widetilde{c^0} \partial_z \widetilde{c^1} |_{-\infty}^{+\infty} + \int_{-\infty}^{+\infty} \kappa_1 \partial_z^2 \widetilde{c^0} \partial_z \widetilde{c^1} dz$$

$$= \int_{-\infty}^{+\infty} \kappa_1 \partial_z^2 \widetilde{c^0} \partial_z \widetilde{c^1} dz, \tag{C2}$$

$$\int_{-\infty}^{+\infty} \kappa_2 \partial_z^4 \widetilde{c^1} \partial_z \widetilde{c^0} dz$$

$$= \int_{-\infty}^{+\infty} \kappa_2 \partial_z \widetilde{c^0} \frac{\partial}{\partial_z} (\partial_z^3 \widetilde{c^1}) dz$$

$$= \kappa_2 \partial_z \widetilde{c^0} \partial_z^3 \widetilde{c^1} |_{-\infty}^{+\infty} - \int_{-\infty}^{+\infty} \kappa_2 \partial_z^3 \widetilde{c^1} \partial_z^2 \widetilde{c^0} dz$$

$$= - \kappa_2 \partial_z^2 \widetilde{c^0} \partial_z^2 \widetilde{c^1} |_{-\infty}^{+\infty} + \int_{-\infty}^{+\infty} \kappa_2 \partial_z^2 \widetilde{c^1} \partial_z^3 \widetilde{c^0} dz$$

$$= \kappa_2 \partial_z^3 \widetilde{c^0} \partial_z \widetilde{c^1} |_{-\infty}^{+\infty} - \int_{-\infty}^{+\infty} \kappa_2 \partial_z \widetilde{c^1} \partial_z^4 \widetilde{c^0} dz$$

$$= - \int_{-\infty}^{+\infty} \kappa_2 \partial_z \widetilde{c^1} \partial_z^4 \widetilde{c^0} dz. \tag{C3}$$

Eq. (C1) + Eq. (C2) + Eq.(C3)

$$= \int_{-\infty}^{+\infty} \left[-f_{,\bar{c}}(\widetilde{c^0}) + \kappa_1 \partial_z^2 \widetilde{c^0} - \kappa_2 \partial_z^4 \widetilde{c^0} \right] \partial_z \widetilde{c^1} dz$$

$$= \int_{-\infty}^{+\infty} -\widetilde{\mu^0} \partial_z \widetilde{c^1} dz = 0.$$

Therefore,

$$\int_{-\infty}^{+\infty} \widetilde{\mu^1} \partial_z \widetilde{c^0} dz = \widetilde{\mu^1} [\widetilde{c^0}(+\infty) - \widetilde{c^0}(-\infty)] = -\sigma \kappa,$$

$$\sigma = \int_{-\infty}^{+\infty} \left[\kappa_1 (\partial_z \widetilde{c^0})^2 + 2\kappa_2 (\partial_z^2 \widetilde{c^0})^2 \right] dz.$$

In the order-3 ECH model, for straight interfaces with concentration variation along, for example, only the z direction, the interfacial energy σ can be expressed as $\int_z (\kappa_1^{\text{eff}} |\nabla c|^2 + 2\kappa_2^{\text{eff}} |\nabla^2 c|^2) dz$. This corresponds to Eq. (24) in the main text.

APPENDIX D: FREE-ENERGY FUNCTIONAL IN ORDER-3 (-5) MODELS AND ONE- (TWO-) MODE SWIFT-HOHENBERG MODELS

This Appendix describes similarities and differences between the order-3(-5) models and the one- (two-) mode Swift-Hohenberg (SH) models.

1. Comparison between the order-3 model and the one-mode SH model

The free-energy functional of the one-mode SH model is given by [64]

$$F = \int_V \left\{ \frac{\phi}{2} [\alpha + \lambda(q_0{}^2 + \nabla^2)^2]\phi + \frac{g}{4}\phi^4 \right\} dV,$$

where α, λ, and g are constants, q_0 is the magnitude of the critical wave vector, and ϕ is the field variable related to the density field of the system. This free-energy functional constitutes the one-mode SH equation, and it results in the minimization of energy by the formation of periodic structures with a critical wave vector. Its dimensionless form is

$$F = \int_V \left[-\frac{(\varepsilon - 1)\psi^2}{2} + \frac{\psi^4}{4} - |\nabla \psi|^2 + \frac{1}{2}|\nabla^2 \psi|^2 \right] dV.$$

Here ε is a reduced parameter and is equal to $-\frac{\alpha}{\lambda q_0{}^4}$, while the field variable is $\psi = \phi \sqrt{\frac{g}{\lambda q_0{}^4}}$. For the order-3 model, in order to compare with the one-mode SH model, a Landau polynomial is used as the bulk free energy instead of the regular solution model. Therefore, the total effective free energy of the order-3 model is

$$F_{\text{eff}} = \int_V \left[-Ac^2 + Bc^4 - \frac{D_1}{2M}c(1-c) + \frac{\kappa_{1_{\text{eff}}}}{2}|\nabla c|^2 \right.$$

$$\left. + \frac{\kappa_{2_{\text{eff}}}}{2}|\nabla^2 c|^2 \right] dV.$$

We now use a one-mode approximation as the compositional profile to derive the analytical expression of free energy as a function of wave vector k in patterning regimes of the two models. In the patterning regime, we assume a 1D parametric function $c = \bar{c} + a \sin(kx)$ as the local composition of B, a is the amplitude, and $\bar{c}$ is the nominal composition of the system. We then derive the effective free energy per unit length $f_{\text{eff}}(k)$ and the minimum of $f_{\text{eff}}(k_c)$ at k_c. The difference between these two terms, in the one-mode SH model ($k_c^2 = 1$), is

$$\Delta f(k) = f(k) - f(k_c) = \frac{a^2}{4}(k^2 - 1)^2.$$

In the order-3 model,

$$\Delta f_{\text{eff}}(k) = f_{\text{eff}}(k) - f_{\text{eff}}(k_c) = \frac{\kappa_2^{\text{eff}} a^2}{4}(k^2 - k_c^2)^2,$$

$$k_c^2 = -\frac{\kappa_1^{\text{eff}}}{2\kappa_2^{\text{eff}}}.$$

Assuming amplitude a is independent of the wave vector and remains a constant, they both show a parabolic relation between free-energy density and k^2. This expression corresponds to Eq. (26) in the main text.

2. Comparison between the order-5 model and the two-mode SH model

To improve the accuracy of solid-liquid interface properties obtained from quantitative PFC models, a two-mode SH model was proposed, including a second critical wave vector in addition to the primary one [75],

$$F = \int_V \left\{ \frac{\phi}{2} \{\alpha + \lambda(q_0{}^2 + \nabla^2)^2[(q_1{}^2 + \nabla^2)^2 + r_1]\}\phi + \frac{g}{4}\phi^4 \right\} dV,$$

where q_1 is the wave vector of the second-mode, and r_1 is a constant. By varying r_1, the relative amplitude between the primary and secondary modes can be adjusted. The dimensionless two-mode SH model has a free-energy potential of the form

$$F = \int_V \left[\frac{A\psi^2}{2} + \frac{\psi^4}{2} - B|\nabla\psi|^2 + \frac{C}{2}|\nabla^2\psi|^2 - \frac{D}{2}|\nabla^3\psi|^2 + \frac{1}{2}|\nabla^4\psi|^2 \right] dV, \quad (D1)$$

where $A = -\varepsilon + R_1 + Q_1{}^4$, $B = R_1 + Q_1{}^2 + Q_1{}^4$, $C = 1 + R_1 + 4Q_1{}^2 + Q_1{}^4$, $D = 2 + 2Q_1{}^2$, $\varepsilon = -\frac{\alpha}{\lambda q_0{}^8}$, $R_1 = \frac{r_1}{q_0{}^8}$, and $Q_1 = \frac{q_1}{q_0}$. R_1 and Q_1 give the freedom to change the relative amplitude and wave vector of the primary and secondary modes. For the order-5 model, the effective potential is [see Eq. (13)]

$$F_{\text{eff}} = \int_V \left[f_{\text{bulk}}^{\text{eff}}(c) + \frac{\kappa_1^{\text{eff}}}{2}|\nabla c|^2 + \frac{\kappa_2^{\text{eff}}}{2}|\nabla^2 c|^2 - \frac{D_4}{2M}|\nabla^3 c|^2 + \frac{D_5}{2M}|\nabla^4 c|^2 \right] dV. \quad (D2)$$

Comparing Eqs. (D1) and (D2), it is noted that all coefficients of the compositional derivative terms in the two-mode SH model and the order-5 model have the same signs (recall that $\kappa_1^{\text{eff}} < 0$ in the patterning regime). A direct mapping of our order-5 model onto the two-mode SH model is, however, not possible. In the two-mode SH model, coefficients are dependent on the relative amplitude and wavelength of the secondary and the primary modes, and such a constraint is not applied to the order-5 model. Furthermore, this later model uses more independent parameters than the two-mode SH model.

---

[1] G. Nicolis, *Self-Organization in Nonequilibrium Systems: From Dissipative Structures to Order through Fluctuations* (Wiley, New York, 1977).

[2] M. C. Cross and P. C. Hohenberg, Rev. Mod. Phys. **65**, 851 (1993).

[3] M. Cross and H. Greenside, *Pattern Formation and Dynamics in Nonequilibrium Systems* (Cambridge University Press, Cambridge, 2009).

[4] N. Ghoniem and D. Walgraef, Instabilities and self-organization in materials: Volume I: Fundamentals of nanoscience, *Volume II: Applications in Materials Design and Nanotechnology* (Oxford University Press, Oxford, 2008), Vol. 1.

[5] J. H. Evans, Nature (London) **229**, 403 (1971).

[6] K. Krishan, Philos. Mag. A **45**, 401 (1982).

[7] K. Krishan, Radiat Eff. **66**, 121 (1982).

[8] N. M. Ghoniem, D. Walgraef, and S. J. Zinkle, J. Comput. Aided Mater. Des. **8**, 1 (2001).

[9] R. S. Nelson, J. A. Hudson, and D. J. Mazey, J. Nucl. Mater. **44**, 318 (1972).

[10] E. C. Aifantis, Int. J. Eng. Sci. **33**, 2161 (1995).

[11] F. Ren, S. N. Arshad, P. Bellon, R. S. Averback, M. Pouryazdan, and H. Hahn, Acta Mater. **72**, 148 (2014).

[12] R. A. Enrique and P. Bellon, Phys. Rev. B **70**, 224106 (2004).

[13] L. Luneville, K. Mallick, V. Pontikis, and D. Simeone, Phys. Rev. E **94**, 052126 (2016).

[14] G. Gompper and M. Kraus, Phys. Rev. E **47**, 4289 (1993).

[15] R. S. Averback and T. D. de la Rubia, in *Solid State Physics—Advances in Research and Applications* (Academic, Cambridge, MA, 1998), pp. 281.

[16] G. Schmitz, J. C. Ewert, F. Harbsmeier, M. Uhrmacher, and F. Haider, Phys. Rev. B **63**, 224113 (2001).

[17] E. Camus, C. Abromeit, F. Bourdeau, N. Wanderka, and H. Wollenberger, Phys. Rev. B **54**, 3142 (1996).

[18] P. Krasnochtchekov, R. S. Averback, and P. Bellon, Phys. Rev. B **72**, 174102 (2005).

[19] S. W. Chee, B. Stumphy, N. Q. Vo, R. S. Averback, and P. Bellon, Acta Mater. **58**, 4088 (2010).

[20] M. Bachhav, G. R. Odette, and E. A. Marquis, Scr. Mater. **74**, 48 (2014).

[21] C. Pareige, V. Kuksenko, and P. Pareige, J. Nucl. Mater. **456**, 471 (2015).

[22] W.-Y. Chen, Y. Miao, Y. Wu, C. A. Tomchik, K. Mo, J. Gan, M. A. Okuniewski, S. A. Maloy, and J. F. Stubbins, J. Nucl. Mater. **462**, 242 (2015).

[23] E. R. Reese, M. Bachhav, P. Wells, T. Yamamoto, G. R. Odette, and E. A. Marquis, J. Nucl. Mater. **500**, 192 (2018).

[24] J.-H. Ke, E. R. Reese, E. A. Marquis, G. R. Odette, and D. Morgan, Acta Mater. **164**, 586 (2019).

[25] M. J. Demkowicz, P. Bellon, and B. D. Wirth, MRS Bull. **35**, 992 (2010).

[26] H. H. Andersen, Appl. Phys. **18**, 131 (1979).

[27] A. Gras-Marti and P. Sigmund, Nucl. Instrum. Methods **180**, 211 (1981).

[28] P. C. Hohenberg and B. I. Halperin, Rev. Mod. Phys. **49**, 435 (1977).

[29] G. Martin, Phys. Rev. B **30**, 1424 (1984).

[30] R. A. Enrique, K. Nordlund, R. S. Averback, and P. Bellon, J. Appl. Phys. **93**, 2917 (2003).

[31] G. Demange, E. Antoshchenkova, M. Hayoun, L. Lunéville, and D. Simeone, J. Nucl. Mater. **486**, 26 (2017).

[32] R. A. Enrique and P. Bellon, Phys. Rev. Lett. **84**, 2885 (2000).

[33] F. Liu and N. Goldenfeld, Phys. Rev. A **39**, 4805 (1989).

[34] L. Leibler, Macromolecules **13**, 1602 (1980).

[35] D. Simeone, G. Demange, and L. Luneville, Phys. Rev. E **88**, 032116 (2013).

[36] D. Simeone, G. J. Thorogood, G. L. Murphy, A. Forestier, P. Garcia, and L. Luneville, J. Appl. Phys. **125**, 065103 (2019).

[37] L. Luneville, P. Garcia, and D. Simeone, Phys. Rev. Lett. **124**, 085701 (2020).

[38] J. Bialké, J. T. Siebert, H. Löwen, and T. Speck, Phys. Rev. Lett. **115**, 098301 (2015).

[39] A. Patch, D. M. Sussman, D. Yllanes, and M. C. Marchetti, Soft Matter **14**, 7435 (2018).

[40] M. Seul and D. Andelman, Science **267**, 476 (1995).

[41] H. M. McConnell, in *Annual Review of Physical Chemistry* (Annual Reviews, Palo Alto, CA, 1991), p. 171.

[42] T. D. Delarubia, R. S. Averback, H. Hsieh, and R. Benedek, J. Mater. Res. **4**, 579 (1989).

[43] H. Zhu, R. S. Averback, and M. Nastasi, Philos. Mag. A **71**, 735 (1995).

[44] R. A. Enrique and P. Bellon, Phys. Rev. B **60**, 14649 (1999).

[45] J. W. Cahn and J. E. Hilliard, J. Chem. Phys. **28**, 258 (1958).

[46] T. A. Abinandanan and F. Haider, Philos. Mag. A **81**, 2457 (2001).

[47] Y. S. Lee, C. P. Flynn, and R. S. Averback, Phys. Rev. B **60**, 881 (1999).

[48] G. R. Odette, T. Yamamoto, and D. Klingensmith, Philos. Mag. **85**, 779 (2005).

[49] C. J. Permann *et al.*, SoftwareX **11**, 100430 (2020).

[50] See Supplemental Material at http://link.aps.org/supplemental/10.1103/PhysRevB.103.104110 for the time evolution of concentration field c_B with the order-17 ECH model and steady-state microstructures with adaptive meshing.

[51] T. Barkar, L. Höglund, J. Odqvist, and J. Ågren, Comput. Mater. Sci. **143**, 446 (2018).

[52] P. Maini, K. Painter, and H. P. Chau, J. Chem. Soc., Faraday Trans. **93**, 3601 (1997).

[53] S. Kondo and T. Miura, Science **329**, 1616 (2010).

[54] H. S. Greenside and W. M. Coughran, Phys. Rev. A **30**, 398 (1984).

[55] S. Sánchez Pérez-Moreno, S. Ruiz Chavarría, and G. Ruiz Chavarría, in *Experimental and Computational Fluid Mechanics*, edited by J. Klapp and A. Medina (Springer International, Cham, 2014), p. 409.

[56] J. W. Gibbs, Am. J. Sci. **s3-16**, 441 (1878).

[57] K. Ahmed and A. El-Azab, Mater. Theor. **2**, 1 (2018).

[58] T. Hochrainer and A. El-Azab, Philos. Mag. **95**, 948 (2015).

[59] N. Provatas and K. Elder, *Phase-Field Methods in Materials Science and Engineering* (Wiley-VCH, Hoboken, NJ, 2010).

[60] R. DeHoff, *Thermodynamics in Materials Science*, 2nd ed. (Taylor & Francis, London, 2006).

[61] S. Hermann, D. De Las Heras, and M. Schmidt, Phys. Rev. Lett. **123**, 268002 (2019).

[62] K. R. Elder, M. Grant, N. Provatas, and J. M. Kosterlitz, Phys. Rev. E **64**, 021604 (2001).

[63] K. R. Elder, M. Katakowski, M. Haataja, and M. Grant, Phys. Rev. Lett. **88**, 245701 (2002).

[64] K. R. Elder and M. Grant, Phys. Rev. E **70**, 051605 (2004).

[65] R. Kirchheim, Acta Mater. **55**, 5129 (2007).

[66] R. Kirchheim, Acta Mater. **55**, 5139 (2007).

[67] G. Tegze, L. Gránásy, G. I. Tóth, F. Podmaniczky, A. Jaatinen, T. Ala-Nissila, and T. Pusztai, Phys. Rev. Lett. **103**, 035702 (2009).

[68] A. Nourian-Avval and E. Asadi, Comput. Mater. Sci. **145**, 224 (2018).

[69] B. Stumphy, S. W. Chee, N. Q. Vo, R. S. Averback, P. Bellon, and M. Ghafari, J. Nucl. Mater. **453**, 66 (2014).

[70] B. Stumphy, R. S. Averback, and P. Bellon, J. Mater. Res. **30**, 170 (2015).

[71] S. Dubey and A. El-Azab, J. Appl. Phys. **114**, 124901 (2013).

[72] J. B. Piochaud, M. Nastar, F. Soisson, L. Thuinet, and A. Legris, Comput. Mater. Sci. **122**, 249 (2016).

[73] J. V. Andersen and O. G. Mouritsen, Phys. Rev. Lett. **65**, 440 (1990).

[74] S. Katz, J. L. Lebowitz, and H. Spohn, Phys. Rev. B **28**, 1655 (1983).

[75] E. Asadi and M. Asle Zaeem, JOM **67**, 186 (2015).